

HIGH ORDER UNFITTED FINITE ELEMENT DISCRETIZATIONS FOR EXPLICIT BOUNDARY REPRESENTATIONS

PERE A. MARTORELL^{1,*} AND SANTIAGO BADIA^{1,2}

ABSTRACT. When modeling scientific and industrial problems, geometries are typically modeled by explicit boundary representations obtained from computer-aided design software. Unfitted (also known as embedded or immersed) finite element methods offer a significant advantage in dealing with complex geometries, eliminating the need for generating unstructured body-fitted meshes. However, current unfitted finite elements on nonlinear geometries are restricted to implicit (possibly high-order) level set geometries. In this work, we introduce a novel automatic computational pipeline to approximate solutions of partial differential equations on domains defined by explicit nonlinear boundary representations. For the geometrical discretization, we propose a novel algorithm to generate quadratures for the bulk and surface integration on nonlinear polytopes required to compute all the terms in unfitted finite element methods. The algorithm relies on a nonlinear triangulation of the boundary, a kd-tree refinement of the surface cells that simplify the nonlinear intersections of surface and background cells to simple cases that are diffeomorphically equivalent to linear intersections, robust polynomial root-finding algorithms and surface parameterization techniques. We prove the correctness of the proposed algorithm. We have successfully applied this algorithm to simulate partial differential equations with unfitted finite elements on nonlinear domains described by computer-aided design models, demonstrating the robustness of the geometric algorithm and showing high-order accuracy of the overall method.

Keywords: Unfitted finite elements, embedded finite elements, computer-aided design, non-uniform rational basis splines, Bernstein-Bézier basis, surface-surface-intersection, computational geometry, immersed boundaries, nonlinear boundary representations.

1. INTRODUCTION

A wide range of industrial and scientific applications requires solving partial differential equations (PDEs) on complex domains. These domains are commonly enclosed by boundary representation (BREP) models and generated in computer-aided design (CAD) software. CAD models are described by non-uniform rational basis splines (NURBS) and boolean operations like constructive solid geometry (CSG). Due to the high-order nature of NURBS, it becomes essential to employ specialized tools capable of efficiently handling numerical simulations on these complex domains.

Despite the enduring popularity of body-fitted meshes in traditional simulation pipelines, they exhibit significant limitations. The generation of body-fitted unstructured mesh generation relies on manual intervention, resulting in significant bottlenecks in the process [1], especially when dealing with high-order representations. Additionally, simulating PDEs on body-fitted meshes with distributed memory machines necessitates mesh partitioning strategies based on graph partition techniques. These algorithms are inherently sequential and demand extensive memory resources [2]. Consequently, the mesh partitioning process represents a major bottleneck in the simulation pipeline and cannot be automated in general.

Unfitted finite element methods (FEMs), also known as embedded or immersed FEMs, offers a solution to the mesh generation bottlenecks by eliminating the need for body-fitted meshes. Unfitted methods rely on a simple background mesh, such as a uniform or adaptive Cartesian mesh. Traditionally, unfitted methods utilize implicit descriptions (level sets) of geometries or handle explicit representations using low order quadratures (e.g., using composite quadratures on adapted meshes [3]) that do not preserve sharp features. The algorithms in [4] compute quadratures for oriented linear triangulations as boundary

¹ CIMNE, Centre Internacional de Mètodes Numèrics a l'Enginyeria, Campus Nord, 08034 Barcelona, Spain.

² School of Mathematics, Monash University, Clayton, Victoria, 3800, Australia.

* Corresponding author.

E-mails: pamartorell@cimne.upc.edu (PM) santiago.badia@monash.edu (SB).

representations (a.k.a. Stereolithography (STL)) without perturbing the geometry, preserving sharp features up to machine precision.

On the other side, several approaches have been introduced to combine unfitted methods with high-order implicit representations of geometries. One notable example is the methodology in [5], which has been gradually improved in subsequent works, including [6–9]. These advancements have even extended to handling BREP models in [10]. Other important contributions are [11, 12] and references therein. However, it is worth noting that these methods still rely on level set representations.

In embedded FEMs the small cut cell problem is a significant limitation extensively discussed in the literature [13]. This problem arises when the intersection between physical and background domain cells becomes arbitrarily small, leading to ill-conditioning issues in the numerical solution. Although various techniques have been proposed to address this problem, only a few have demonstrated robustness and optimal convergence. One approach is the ghost penalty method [14], which is utilized in the CutFEM packages [15]. Alternatively, cell agglomeration techniques present a viable option to ensure robustness concerning the cut cell location, which were originally applied to discontinuous Galerkin (DG) methods [16, 17]. Extensions to the C^0 Lagrangian finite element (FE) have been introduced in [18], while mixed methods have been explored in [19], where the aggregated finite element method (AgFEM) term was coined. AgFEM exhibits good numerical qualities, including stability, bounds on condition numbers, optimal convergence, and continuity concerning data. Distributed implementations have been exploited in [20, 21], also AgFEM has been extended to h -adaptive meshes [22] and higher-order FE with modal C^0 basis in [23]. In [24], a novel technique combining ghost penalty methods with AgFEM was proposed, offering reduced sensitivity to stabilization parameters.

The development of isogeometric analysis (IGA) over the past two decades has been driven by the goal of improving the interaction between CAD and computer-aided engineering (CAE) [1]. While IGA techniques are suitable for PDEs on boundaries, they cannot readily handle PDEs in the volume of a CAD representation of the domain. Standard CAD representations are 2-variate (boundary representations) and they do not provide a parameterization of the volume. To overcome this limitation, some works [25–28] propose constructing volume parametrizations based on Bernstein-Bézier basis using the Bézier projection techniques described in [29]. Nevertheless, these approaches still rely on high-order unstructured meshes, thereby inheriting the known limitations associated with them, such as tangling issues, lack of parallelization, and global graph partition bottlenecks.

Similarly to unfitted FE methods, immersed IGA [30–32] eliminates the need for unstructured meshes by utilizing the intersection of a background mesh. These methods utilize integration techniques for complex domains, including dimension reduction of integrands [33, 34], i.e., integrating over lines and surfaces. The precision of these methods is bounded by the approximation algorithms used on the *trimming curves*, which represent surface-surface intersections [9, 35] resulting from boolean CSG on the CAD models.

One of the primary challenges in the CAD to CAE paradigm is the approximation of trimming curves [36–38]. Trimming curves, in general, cannot be represented in the intersected surface patches. In the literature, there is a wide range of strategies to approximate trimming curves, see [39, 40] and references therein. These strategies can be categorized into analytical methods, lattice evaluation methods, subdivision methods, marching methods, or a combination thereof. The representation of the approximated trimming curves is also extensively studied. Once the trimming curves are approximated, various techniques can be employed. Untrimming techniques [27, 28, 41–43] are one approach, which involves a conformal reparametrization of the original surface. Another approach is the direct integration onto trimmed surfaces [34, 44].

In this work, we propose a computational framework that combines unfitted FEM and implicit CAD representations of the geometry. In order to do this, we propose a novel approach to numerically integrate on unfitted cut cells that are intersected by domains bounded by a high-order BREPs. Our method involves approximating the geometry using a set of Bézier patches, utilizing Bézier projection methods [45]. By leveraging the properties of Bézier curves, we can efficiently perform intersections. We can reduce the complexity of the collision interrogations and tangling prediction through the convex hull property. The variational diminishing property of Bézier curves enables root isolation for determining the intersection points [46]. We can employ efficient multivariate root-finding techniques [47, 48] for polynomials on nonrational Bézier patches. To build an intersection method for nonlinear boundary representations, we

combine the intersection techniques with partition techniques typically used in level set methods [5] and linear polytopal intersection [4]. We propose a kd-tree refinement of the surface Bézier triangulation that reduces nonlinear intersections against background cells to simple situations that are diffeomorphically equivalent to linear intersections. This allows us to handle the complexity of intersecting high-order geometries efficiently. Furthermore, we can approximate these intersections with a set of Bézier patches using least-squares techniques based on [49].

With the intersection method established, we are then able to integrate on the surface of these polytopes to solve PDEs on high-order unfitted FE meshes. We employ moment-fitting techniques based on Stokes theorem [23, 33] to ensure accurate and stable integration. By utilizing these techniques, we can effectively handle the integration process on high-order unfitted FE meshes, allowing for the solution of PDEs in domains bounded by complex high-order BREPs.

The outcomes of this work are as follows:

- An automatic computational framework that relies on a robust and accurate intersection algorithm for background cells and Bézier patches of arbitrary order (briefly described above), and the mathematical analysis of the correctness of the algorithm.
- Accuracy and robustness numerical experimentation of the intersection algorithm. The algorithms exhibit optimal convergence rates of the surface and volume integration. These errors are robust concerning the relative position of the background cells and the BREP.
- The numerical experimentation of a high-order unfitted FE method for high-order BREPs with analytical benchmarks. The results demonstrate optimal hp -convergence of the error norms.
- The demonstration of the application of the methods for problems defined in CAD geometries.

The outline of this article is as follows. Firstly, in Sec. 2, we introduce the unfitted FE methods and their requirements for handling high-order BREPs. Next, in Sec. 3, we provide the proposed geometric algorithms for computing the nonlinear intersections between background cells and oriented high-order BREPs, along with a surface parametrization method for integration purposes. Then, in Sec. 4, we present the numerical results obtained from applying the proposed method, including accuracy and robustness of the intersections, benchmark tests for validation of the unfitted FE pipeline, and simulations on CAD geometries. Finally, in Sec. 5, we draw the main conclusions and future work lines.

2. UNFITTED FINITE ELEMENT METHOD

2.1. Unfitted finite element formulations. Let us consider an open Lipschitz domain $\Omega \in \mathbb{R}^3$ in which we want to approximate a system of PDEs. An oriented high-order surface mesh \mathcal{B} defines the domain boundary $\partial\Omega$ and encloses the domain interior. The PDEs usually involve Dirichlet boundary conditions on Γ_D and Neumann boundary conditions on Γ_N , where $\partial\Omega \doteq \Gamma_D \cup \Gamma_N$ and $\Gamma_D \cap \Gamma_N = \emptyset$. These subsets, Γ_D and Γ_N , correspond to geometric discretizations of \mathcal{B}_D and \mathcal{B}_N , resp., such that $\mathcal{B} \equiv \mathcal{B}_D \cup \mathcal{B}_N$.

The principal motivation of this work is to enable the utilization of grid-based unfitted numerical schemes that can be automatically generated from the oriented high-order surface mesh \mathcal{B} . This approach is valuable in industrial and scientific applications. We can alleviate the geometric constraints associated with body-fitted meshes by employing embedded discretization techniques. These techniques utilize a background partition \mathcal{T}^{bg} defined over an arbitrary artificial domain $\Omega^{\text{art}} \supseteq \Omega$. The artificial domain can be a simple bounding box containing Ω , dramatically simplifying the computation of \mathcal{T}^{bg} compared to a body-fitted partition of Ω . In this work, we adopt a Cartesian mesh \mathcal{T}^{bg} for the sake of simplicity, although the proposed approach can readily be used on other types of background meshes, such as tetrahedral structured meshes obtained through simplex decomposition or adaptive mesh refinement (AMR) techniques.

The abstract exposition of unfitted formulations considered in this work is general and encompasses various unfitted FE techniques from the literature. These techniques include the extended finite element method (XFEM) [50], designed for handling unfitted interface problems. In order to have robustness with respect to small cut cells, the cutFEM method [15] and the finite cell method [51] add additional terms to enhance stability. The AgFEM [18] provides robustness via a discrete extension operator from interior to cut cells. Since DG methods can work on polytopal meshes, combined with cell aggregation [52], they are also robust unfitted FE techniques.

The definition of FE spaces on unfitted meshes requires a cell classification. The background cells $K \in \mathcal{T}^{\text{bg}}$ with a null intersection with Ω are classified as exterior cells and are denoted as \mathcal{T}^{out} . These exterior cells, which have no contribution to functional discretization and can be discarded. The active mesh, denoted as $\mathcal{T} = \mathcal{T}^{\text{bg}} \setminus \mathcal{T}^{\text{out}}$, represents the relevant mesh for the problem (Fig. 1). The unfitted FE techniques stated above utilize FE spaces defined on \mathcal{T} to construct the finite-dimensional space V . This space approximates the solution and tests the weak form of PDEs. An abstract unfitted FE problem reads as follows: find $u \in V$ such that

$$a(u, v) = l(v), \quad \forall v \in V,$$

where

$$a(u, v) = \int_{\Omega} L_{\Omega}(u, v) d\Omega + \int_{\Gamma_D} L_D(u, v) d\Gamma + \int_{\mathcal{F}} L_{\text{sk}}(u, v) d\Gamma,$$

and

$$l(v) = \int_{\Omega} F_{\Omega}(v) d\Omega + \int_{\Gamma_N} F_N(v) d\Gamma + \int_{\Gamma_D} F_D(v) d\Gamma.$$

The bulk terms L_{Ω} and F_{Ω} consist of the weak form of the differential operator, the source term, and possibly other numerical stabilization terms. On Γ_D , the operators L_D and F_D represent the enforcement of the Dirichlet boundary conditions, often implemented using Nitsche's method in unfitted formulations. The term F_N on Γ_N represents the Neumann boundary conditions of the given problem. The skeleton of the active mesh \mathcal{F} corresponds to the interior faces of \mathcal{T} , while the term L_{sk} collects additional penalty terms, such as weak continuity enforcement in DG methods or ghost penalty stabilization techniques.

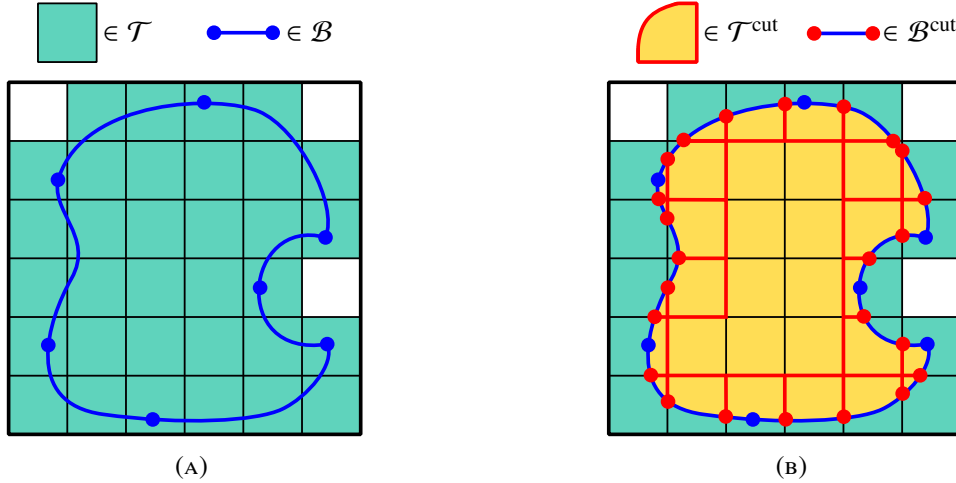


FIGURE 1. Example of the embedded nonlinear domain in 2D. Figure (a) presents a nonlinear oriented skin mesh \mathcal{B} embedded in an active mesh \mathcal{T} . The intersections, computed with the techniques proposed in this work, result in the two-level partitions \mathcal{T}^{cut} and \mathcal{B}^{cut} shown in (b). These partitions are utilized for integrating unfitted formulations. It is important to note that the intersections in 2D are points that can be represented exactly. However, the intersections in 3D are trimming curves that must be approximated in general.

Since FE methods are piecewise polynomials, integrating these terms requires a cell-wise decomposition for both bulk and surface contributions. However, to accurately respect the geometry and solve the PDE on the proper domain, it is necessary to perform these integrals within the interiors of the domains. In particular, we have

$$\int_{\Omega} (\cdot) d\Omega = \sum_{K \in \mathcal{T}} \int_{K \cap \Omega} (\cdot) d\Omega. \quad (1)$$

Due to the inherent characteristics of unfitted FE methods, the surface mesh \mathcal{B} is not the boundary restriction of the background mesh \mathcal{T} , which defines the cell-wise polynomial FE functions. Consequently, to integrate the boundary terms on \mathcal{B} , we must compute a cell-wise integral as follows:

$$\int_{\Gamma_*} (\cdot) d\Gamma = \sum_{K \in \mathcal{T}} \sum_{F \in \mathcal{B}_*} \int_{F \cap K} (\cdot) d\Gamma, \quad * \in \{D, N\}. \quad (2)$$

It is important to note that, in general, we do not need to restrict the integrals on the skeleton terms L_{sk} to the domain interior. In most formulations, e.g., ghost penalty and DG methods, one integrates these terms on the entire face skeleton. Therefore, in the unfitted FE methods, we must give particular attention to the geometrical operations involving $K \cap \Omega$ and $K \cap \mathcal{B}$ (or more specifically, \mathcal{B}_N and \mathcal{B}_D). However, the methodology described below also handles $F \cap \Omega$ for $F \in \mathcal{F}$, in case it is required.

2.2. Geometrical ingredients for unfitted finite elements. This section aims to describe the geometrical entities that we need to compute the integrals (1)-(2) of unfitted FE formulations. These entities are easier to compute than unstructured meshes in body-fitted formulations. Our geometrical framework involves intersection algorithms that are cell-wise, and so, embarrassingly parallel. Since the FE spaces are defined on background meshes, the cut meshes do not require to be conforming or shape-regular.

The input of our geometrical framework is an oriented mesh of non-rational triangular Bézier elements \mathcal{B} whose interior is the domain Ω . Each triangle $F \in \mathcal{B}$ is the image of a Bézier map $\phi_F : \hat{F} \rightarrow F$ of order q acting on a reference triangle $\hat{F} \subset \mathbb{R}^2$.

In the following exposition, we use $\hat{\xi}$ to represent the coordinate system of the reference space of \hat{F} and \mathbf{x} to represent the coordinate system of the physical space. Given a set of points \hat{f} in the reference space of \hat{F} we can compute $f \doteq \phi_F(\hat{f})$. Since \hat{F} is diffeomorphic, we can also define f and compute $\hat{f} \doteq \phi_F^{-1}(f)$. Given a function $\hat{\gamma}(\hat{\xi})$ in the reference space of \hat{F} , we can compute $\gamma(\mathbf{x}) \doteq \hat{\gamma} \circ \phi_F^{-1}(\mathbf{x})$. Conversely, we can define $\gamma(\mathbf{x})$ in the physical domain and compute its pull-back $\hat{\gamma}(\hat{\xi}) \doteq \gamma \circ \phi_F(\hat{\xi})$. We will heavily use this notation to transform sets and functions between the reference and physical spaces.

In practical applications, geometries are described through a CAD model \mathcal{B}^{CAD} . Transforming \mathcal{B}^{CAD} into \mathcal{B} generally involves an approximation process, where we can utilize least-squares methods and third-party libraries, e.g., `gmsh` [53]. Next, we perform intersection algorithms between the surface representation and the background mesh, which consist of two steps as follows.

In the first step, we consider the intersection of the triangular Bézier elements that compose the surface $F \in \mathcal{B}$ with the background cells $K \in \mathcal{T}$. According to (2), the resulting mesh \mathcal{B}^{cut} can be represented as a two-level mesh:

$$\mathcal{B}^{\text{cut}} \doteq \bigcup_{K \in \mathcal{T}} \mathcal{B}_K^{\text{cut}}, \quad \text{where} \quad \mathcal{B}_K^{\text{cut}} \doteq \{F \cap K : F \in \mathcal{B}\}.$$

\mathcal{B}^{cut} is a partition of \mathcal{B} composed of general *nonlinear polytopes* (see Fig. 2). We define a nonlinear polytope as the image of a polytope under a diffeomorphic map.

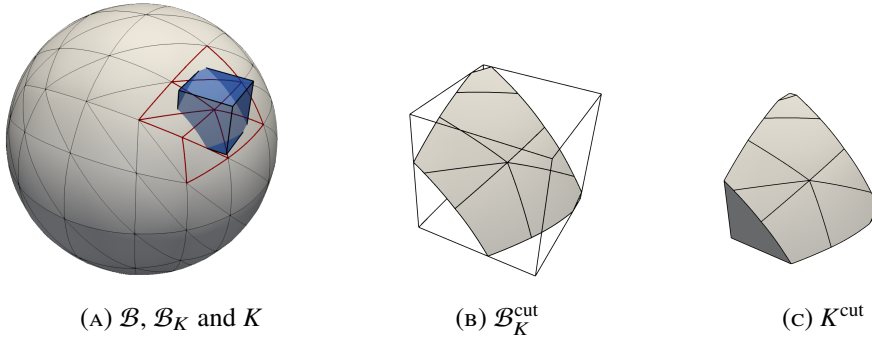


FIGURE 2. Representation of the surface $\mathcal{B} \doteq \partial\Omega$ (see (a)), its intersection $\mathcal{B}_K^{\text{cut}} \doteq \mathcal{B} \cap K$ for a background cell $K \in \mathcal{T}$ (see (b)), and the domain interior of the cell $K^{\text{cut}} \doteq K \cap \Omega$ (see (c)). In order to compute $\mathcal{B}_K^{\text{cut}}$, we identify first the subset of cells $\mathcal{B}_K \subseteq \mathcal{B}$ touching K (see cells with red edges in (a)). Next, for each triangle $F \in \mathcal{B}_K$, we compute the intersection of $F \cap K$ at the reference FE, i.e., we compute $\phi_F^{-1}(F \cap K)$. Finally, we intersect K with the surface portion $\mathcal{B}_K^{\text{cut}}$ to obtain K^{cut} . It is worth to note that $\mathcal{B}_K^{\text{cut}} \subset \partial K^{\text{cut}}$.

In the second step, we compute a mesh of general nonlinear polyhedra that represent the domain interior of background cells (see Sec. 3.6):

$$\mathcal{T}^{\text{cut}} \doteq \bigcup_{K \in \mathcal{T}} K^{\text{cut}}, \quad \text{where} \quad K^{\text{cut}} \doteq K \cap \Omega.$$

The surface cut cells in $\mathcal{B}_K^{\text{cut}}$ are nonlinear polygons that can be split into simplices. A simplex decomposition of the volumetric cells in \mathcal{T}^{cut} is much more complex and expensive. Instead, we avoid a trivariate representation of \mathcal{T}^{cut} and instead rely on a bivariate representation of $\partial\mathcal{T}^{\text{cut}}$. We consider a boundary representation (often abbreviated B-rep or BREP in solid modeling and computer-aided design) of K^{cut} as the interior of an oriented closed surface represented as the collection of connected oriented surface elements, i.e.:

$$\partial K^{\text{cut}} = (\partial K)^{\text{cut}} \cup \mathcal{B}_K^{\text{cut}}, \quad (\partial K)^{\text{cut}} \doteq \bigcup_{F \in \Lambda^2(K)} F \cap \Omega. \quad (3)$$

2.3. Integration methods for cut cells. For the computation of the volume integrals in (1), since we define cut cells by its boundary representation in (3), we compute the integration of polynomials on volume cut cells by transforming them into surface integrals via Stokes theorem [23, 33]. Let us denote r th order polynomial differential k -forms in \mathbb{R}^3 with $\mathcal{P}_r \Lambda^k(\mathbb{R}^3)$ and d the exterior derivative (see, e.g., [54]). For any $\omega(\mathbf{x}) \in \mathcal{P}_r \Lambda^3(\mathbb{R}^3)$, one can readily find $\sigma \in \mathcal{P}_{r+1} \Lambda^2(\mathbb{R}^3)$ such that $\omega(\mathbf{x}) = d\sigma(\mathbf{x})$, due to the exactness of the polynomial de Rham complex. Using Stokes theorem, one gets:

$$\begin{aligned} \int_{K^{\text{cut}}} \omega &= \int_{\partial K^{\text{cut}}} \sigma = \int_{\mathcal{B}_K^{\text{cut}}} \sigma + \int_{(\partial K)^{\text{cut}}} \sigma = \sum_{F \in \mathcal{B}_K} \int_{F \cap K} \sigma + \sum_{F \in \Lambda^2(K)} \int_{F \cap \Omega} \sigma \\ &= \sum_{F \in \mathcal{B}_K} \int_{\phi_F^{-1}(F \cap K)} \phi_F^*(\sigma) + \sum_{F \in \Lambda^2(K)} \int_{\phi_F^{-1}(F \cap \Omega)} \phi_F^*(\sigma). \end{aligned} \quad (4)$$

where $\phi_F^*(\sigma)$ denotes the pull-back of σ by ϕ_F . In order to create a quadrature on K^{cut} , we combine this expression with a moment-fitting technique. First, we integrate all the elements in the monomial basis for $\mathcal{P}_r(\mathbb{R}^3)$; e.g., given a monomial 3-form $\omega(\mathbf{x}) = x^\alpha y^\beta z^\gamma dx \wedge dy \wedge dz$, we define $\sigma(\mathbf{x}) = \frac{1}{\alpha+1} x^{\alpha+1} y^\beta z^\gamma dy \wedge dz$ (which holds $\omega = d\sigma$) and use (4). After computing these integrals for the monomial basis at each face $F \in \mathcal{B}_K$, we can combine them to compute the integrals of Lagrangian polynomials, use the corresponding nodal interpolation, and end up with a quadrature on the cut cell K^{cut} .

To compute the surface integrals in (2) and the right-hand side of (4), we have several options. One approach is to generate a simplex nonlinear mesh of the boundary of the nonlinear polytopes in \mathcal{T}^{cut} , which is feasible on surfaces. We can use a moment-fitting method to compress the resulting quadrature. E.g., for the integral on $\mathcal{B}_K^{\text{cut}}$, we consider a nonlinear triangulation $\mathcal{S}_{\hat{F}}^{\text{cut}}$ of $\phi_F^{-1}(F \cap K)$ and compute:

$$\int_{\mathcal{B}_K^{\text{cut}}} \sigma = \sum_{F \in \mathcal{B}_K} \sum_{S \in \mathcal{S}_{\hat{F}}^{\text{cut}}} \int_S \phi_F^*(\sigma) = \sum_{F \in \mathcal{B}_K} \sum_{S \in \mathcal{S}_{\hat{F}}^{\text{cut}}} \int_{\hat{F}} \phi_S^* \circ \phi_F^*(\sigma) \quad (5)$$

where we rely on a map $\phi_S : \hat{F} \rightarrow S$ to transform the integral to the reference triangle \hat{F} ; S is a nonlinear triangle in \mathbb{R}^2 because it can have nonlinear edges. We proceed analogously for the surface integral on $(\partial K)^{\text{cut}}$; this is a simpler case, since the surface is already contained in a plane in the physical space.

The edges of $S \in \mathcal{S}_{\hat{F}}^{\text{cut}}$ that result from intersections are implicitly defined. Thus, we must consider an approximation $\tilde{\phi}_S$ of the map ϕ_S in (5). This approximation is detailed in the next section. Since F (and as a result $S \in \mathcal{T}^{\text{cut}}$) is a smooth manifold, the polynomial approximation $\tilde{\phi}_S$ will introduce an error that is reduced by increasing the polynomial order of the approximation or by reducing the diameter of S . In turn, the diameter goes to zero with both the background mesh \mathcal{T} and surface mesh \mathcal{B} characteristic sizes.

Another approach is to integrate the pull-back $\phi_F^*(\sigma)$ of the polynomial differential form σ in (4) on the surface to \hat{F} (which are polynomials of higher order due to the factor $\det(\frac{\partial \phi_F}{\partial \xi})$) that comes from the

pullback) and transform the integral to $\partial\hat{F}$ using Stokes theorem:

$$\begin{aligned} \int_{F \cap K} \sigma &= \int_{\phi_F^{-1}(F \cap K)} \phi_F^*(\sigma) = \int_{\phi_F^{-1}(F \cap K)} d\varrho \\ &= \int_{\partial\phi_F^{-1}(F \cap K)} \varrho = \int_{\phi_F^{-1}(\partial F \cap K)} \varrho, \quad \forall \varrho \in \mathcal{P}_{r+2q}\Lambda^1(\mathbb{R}^2) : d\varrho = \phi_F^*(\sigma). \end{aligned} \quad (6)$$

We note that $\phi_F^*(\sigma) \in \mathcal{P}_{r+2q-1}\Lambda^2(\mathbb{R}^2)$ and the existence of ϱ is assured by the exactness of the polynomial de Rham complex. In this case, we can extract the (nonlinear) edges E of $\partial F \cap K$ and define a map $\phi_E : \hat{E} \rightarrow E$ from ϕ_F . Next, we can compute the integrals in a reference segment, i.e.,

$$\int_{F \cap K} \sigma = \sum_{E \in \partial F \cap K} \int_{\phi_E^{-1}(E)} \varrho.$$

As above, since some edges $E \in \partial F \cap K$ are only implicitly defined, we must consider approximations $\tilde{\phi}_E$ of ϕ_E in (6). However, we do not need to compute approximated surface maps or triangulations of $\phi_F^{-1}(F \cap K)$. Since we approximate each edge separately, and both F and the faces of K are smooth manifolds, a polynomial approximation provides error bounds that vanish by increasing the polynomial order or by reducing the edge sizes; edge sizes also go to zero with both the background mesh \mathcal{T} and surface mesh \mathcal{B} characteristics sizes.

3. INTERSECTION ALGORITHM

In this section, we describe an algorithm that takes a background mesh \mathcal{T} and a high-order oriented surface \mathcal{B} as inputs and returns \mathcal{T}^{cut} and \mathcal{B}^{cut} . This algorithm is robust to the relative position of \mathcal{T} and \mathcal{B} . Moreover, it provides an accurate description of the intersections. We list below the different steps considered in the definition of the algorithm:

- (1) In Sec. 3.1, we describe the nonlinear computations of the singular points utilized in the intersection algorithms. There, we utilize multivariate root-finding techniques [48].
- (2) In Sec. 3.2 and Sec. 3.3, we propose an accurate intersection algorithm for nonlinear polyhedra. It combines refinement strategies (to simplify the nonlinear intersection to simple cases) and linear clipping methods [4].
- (3) Sec. 3.4 describes a partition method for the intersected surface. This partition is composed of standard polytopes and is ready to be parametrized.
- (4) In Sec. 3.5, we introduce a parametrization method for intersected nonlinear polyhedra. This parametrization consists of a combination of least-squares methods [49] and sampling strategies [5]. It returns a set of nonrational Bézier patches.
- (5) In Sec. 3.6, we build the polyhedral representation of the intersected cells. In addition, we provide the tool to parametrize the resulting surface.

We describe a global algorithm that combines the previous algorithms in Sec. 3.7.

3.1. Intersection points. In this section, we perform some intersection algorithms that will be required in our geometrical framework. In order to compute surface intersections, we require the computation of three types of intersections, described below.

Consider an oriented plane π defined by a point \mathbf{x}_π on the plane and its outward normal \mathbf{n}_π . The plane-point distance function can be computed as

$$\gamma_\pi(\mathbf{x}) \doteq \text{dist}(\pi, \mathbf{x}) \doteq (\mathbf{x} - \mathbf{x}_\pi) \cdot \mathbf{n}_\pi, \quad \mathbf{x} \in \mathbb{R}^3. \quad (7)$$

In the following, we will also consider this distance function parametrized in the reference face \hat{F} as $\hat{\gamma}_\pi(\hat{\xi}) \doteq \gamma_\pi \circ \phi_F(\hat{\xi})$. Let us denote by $\text{int}(\gamma_\pi) = \{\mathbf{x} : \gamma_\pi(\mathbf{x}) < 0\}$ the interior of a level set. The zero level set of the distance function is represented by

$$\hat{\gamma}_\pi^0 \doteq \{ \hat{\xi} \in \hat{F} : \text{dist}(\pi, \phi_F(\hat{\xi})) = 0 \}. \quad (8)$$

3.1.1. *Curve-plane intersection.* First, we define the curve-plane intersections as the intersection of an edge $E = \phi_E(\hat{E})$ (which can be described as a diffeomorphic polynomial map on a reference segment \hat{E}) with a plane π (see Fig. 3a). We compute the intersection points in the reference segment \hat{E} as the result of finding:

$$\hat{t} \in \hat{E} : \gamma_\pi \circ \phi_E(\hat{t}) = 0.$$

If $E \in \Lambda^1(F)$, the map $\phi_E : \hat{E} \rightarrow E$ can be readily obtained from the corresponding face map ϕ_F . Since ϕ_E is a polynomial, the computation of \hat{t} involves finding the roots of a univariate polynomial system. One can utilize root isolation techniques combined with standard iterative solvers, e.g., the Newton-Rapson method. As the solution may be not unique, the root isolation techniques in [46] provide the means to find multiple roots by leveraging the variation diminishing property of Bézier curves.

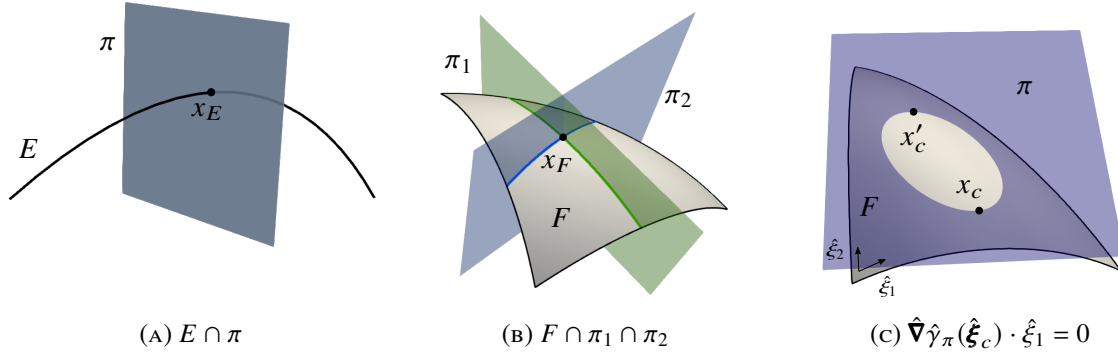


FIGURE 3. Definition of intersection points. The intersection of curves and planes (see (a)) is computed through univariate root-finding methods. The surface-plane-plane intersection points in (b) also represent the intersection of surface-line intersections. The AA critical points in (c) are defined in the reference space of F . These points split the surface-plane intersection curves into monotonic curves in the reference space (see an analogous reference space in Fig. 4a). Both computations, surface-plane-plane intersection points and AA critical points, require solving a bivariate root system.

3.1.2. *Surface-line intersection.* Next, we consider line-surface intersections. Since a line can be represented as the intersection of two half-spaces, we compute surface-line intersections as surface-plane-plane intersections (see Fig. 3b). To compute these intersections, we find:

$$\hat{\xi} \in \hat{F} : \gamma_{\pi_i} \circ \phi_F(\hat{\xi}) = 0, \quad \forall i \in \{1, 2\},$$

where π_1, π_2 are the planes whose intersection is the line we want to intersect. We note that $\hat{\xi} \in \mathbb{R}^2$. It can be checked that this is a system of two bivariate polynomial equations of order q . The roots can be computed using bivariate root-finding algorithms for polynomials. The algorithms described in [48] bound and subdivide the reference domain until the roots are isolated with a given precision. In this work, we adapt the implementation to simplices using the bounding techniques defined in [47].

3.1.3. *Critical points of the zero isosurface of a distance function with respect to an edge.* Finally, we compute the points in which the zero level set curve $\hat{\gamma}_\pi^0$ has a zero directional derivative with respect to a given direction \mathbf{t} (see Fig. 3c). When the direction \mathbf{t} is axis-aligned (AA), we call these points *AA critical points*. These points are obtained as the solution of the following system:

$$\hat{\xi} \in \hat{F} : \hat{\nabla} \hat{\gamma}_\pi(\hat{\xi}) \cdot \mathbf{t} = 0, \quad \hat{\gamma}_\pi(\hat{\xi}) = 0,$$

which is again a system of two bivariate polynomial equations of order q and can be computed as above. We note that the critical points are defined in the reference space. Thus, we take the gradient in the reference space.

3.2. Nonlinear trimming surface. Given a face $F \in \mathcal{B}_K$, we consider its intersection against a cell $K \in \mathcal{T}_h$. The objective is to create a partition of \mathcal{B}_K by splitting its faces by intersection against the background cells $K \in \mathcal{T}_h$. We consider \mathcal{T}_h to be a partition of Ω_{art} in a pointwise sense, i.e., every $\mathbf{x} \in \Omega_{\text{art}}$ belongs to only one $K \in \mathcal{T}_h$. K is neither open nor closed in general, i.e., each background facet belongs to a single background cell. In particular, given a cell whose closure is $\bar{K} = [x^-, x^+] \times [y^-, y^+] \times [z^-, z^+]$, we define the cell as $K = (x^-, x^+) \times (y^-, y^+) \times (z^-, z^+)$. We refer to [4, Sec. 3.6] for more details. The pointwise partition is required to properly account for the case in which $F \in \mathcal{B}_K$ is (in machine precision) on K ; otherwise, we could be counting more than once the same face F . We utilize the notation K° and \bar{K} to refer to the interior and closure of K , resp.

Assumption 3.1. We assume that $F \cap K^\circ \neq \emptyset$.

In [4], we propose an algorithm that determines whether the assumption holds, i.e., checks if $F \cap \pi_f = F$ for some $f \in \Lambda^2(K)$. Here, $f \in \Lambda^2(K)$ represents a face bounding K and π_f its corresponding half-space. If the assumption does not hold, $F \cap K = F \cap f$, and we perform the intersection in one dimension less, which is a simplification of the one below.

Assumption 3.2. We assume that all intersection queries are well-posed, i.e., they return a finite number of points.

For simplicity in the exposition, we postpone the ill-posed cases till the end of the section.

For each $f \in \Lambda^2(K)$ and its corresponding half-space π_f , we can define the distance function $\hat{\gamma}_{\pi_f}$ in the reference space using (7), which we denote with $\hat{\gamma}_f$ for brevity. We can also consider the zero level set curves $\{\hat{\gamma}_f^0\}_{f \in \Lambda^2(K)}$, using (8), and their intersections:

$$\hat{\gamma}_f^0 \cap \hat{\gamma}_{f'}^0, \quad f, f' \in \Lambda^2(K).$$

We note that the intersection points of these curves are the intersections $\phi_F^{-1}(\pi_f \cap \pi_{f'})$; $\pi_f \cap \pi_{f'}$ contains the edge $e \in \Lambda^1(K)$ such that $e \in f, f'$. We also note that $\hat{\gamma}_f^0 \cap \hat{F}$, $f \in \Lambda^2(K)$, can have several disconnected parts. We represent with $C_f(\hat{F})$ the set of mutually disconnected components of $\hat{\gamma}_f^0 \cap \hat{F}$.

In the following, we want to refine F in such a way that the nonlinear case is *diffeomorphically* equivalent to the linear one. Thus, we can use a linear clipping algorithm to compute the cyclic graph representation of the nonlinear polytope (see [4]). For this purpose, we consider the AA refinement ref_1 of F presented in Alg. 1 and illustrated in Fig. 4. This AA refinement generates a kd -tree partition. A kd -tree is a binary tree that splits a k -dimensional space of each non-leaf node through a hyperplane (see, e.g., [55] for details).

Let us consider the level set curve $\hat{\gamma}_{\varepsilon_d}^0$ associated with the diagonal edge $\varepsilon_d \in \Lambda^1(\hat{F})$. After ref_1 , these edges cannot contain intersection points in their interior. Having intersection points only on AA edges simplifies the exposition of the next algorithms. We cannot do the same for AA edges since new AA edges are generated after each refinement step and new intersections can appear.

Algorithm 1 ref_1 : axis-aligned refinement of invariants

Let us consider a kd -tree partition $\text{ref}_1^0(\hat{F})$ of \hat{F} by refining against

- (1) $\hat{\xi}_1$ -aligned lines that contain the $\hat{\xi}_2$ -aligned critical points of $\hat{\gamma}_f^0$, $f \in \Lambda^2(K)$. Proceed analogously for $\hat{\xi}_2$ -aligned lines and $\hat{\xi}_1$ -aligned critical points.
- (2) $\hat{\xi}_1$ and $\hat{\xi}_2$ -aligned lines containing each intersections $\hat{\gamma}_f^0 \cap \hat{\gamma}_{f'}^0$ and $\hat{\gamma}_f^0 \cap \hat{\gamma}_{\varepsilon_d}^0$, for all $f, f' \in \Lambda^2(K)$.

After this refinement, if $\hat{\gamma}_f^0 \cap \partial \hat{F}_R$, $f \in \Lambda^2(K)$, $\hat{F}_R \in \text{ref}_1^0(\hat{F})$, has more than two intersection points, consider the partition $\text{ref}_1^1(\hat{F}_R)$ by refining against

- (3) AA lines perpendicular to the AA edge $\varepsilon \in \Lambda^1(\hat{F}_R)$ containing each of these intersection points. Next, if $\hat{\gamma}_f \cap \hat{\gamma}_{f'}$ or $\hat{\gamma}_f \cap \hat{\gamma}_{\varepsilon_d}^0$, $f, f' \in \Lambda^2(K)$, intersect more than once $\hat{F}_R \in \text{ref}_1^1 \circ \text{ref}_1^0(\hat{F})$,
- (4) Consider a partition of \hat{F}_R by an AA line that passes between two vertices.

Return the final kd -tree partition $\text{ref}_1(\hat{F})$ after these four steps.

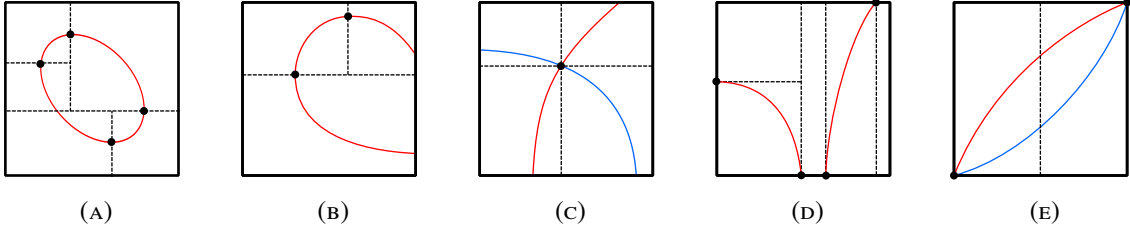


FIGURE 4. Refinement steps of Alg. 1. Step 1 is represented in (a) and (b). Steps 2-4 are represented in (c)-(e), resp. Red and blue dashed lines represent the $\hat{\gamma}_f^0$ and $\hat{\gamma}_{f'}^0$ -curves, resp., $f, f' \in \Lambda^2(K)$. Interior black lines represent the proposed partition of \hat{F} for a given invariant. Solid black lines are the edges of $\Lambda^1(\hat{F})$. There are multiple possible partitions, depending on the order the intersections are processed.

Proposition 3.3. *The number of faces in $\text{ref}_1(\hat{F})$ is bounded.*

Proof. First, we note that there is a limited number of intersections and critical points since ϕ_F is a polynomial. Thus, the number of lines in the refinement strategy is bounded, so the resulting number of faces is also bounded. Furthermore, these points do not change with refinement (the sides of the children faces can only be parallel to the sides of the parent face). Only the intersection points in step (3) do change with refinement. However, we only need to perform step (3) once for the purpose of Prop. 3.4. \square

Proposition 3.4. *After the refinement strategy above, for any $f \in \Lambda^2(K)$, $C_f(\hat{F}_R)$ is a set of smooth connected curves such that: given $\hat{F}_R \in \text{ref}_1(\hat{F})$*

- (i) *the curves in $C_f(\hat{F}_R)$ cannot be tangent to any AA line in $\hat{F}_R \setminus \Lambda^0(\hat{F}_R)$;*
- (ii) *every curve in $C_f(\hat{F}_R)$ is strictly monotonic with respect to the coordinates $(\hat{\xi}_1, \hat{\xi}_2)$, can only intersect once AA segments in $\hat{F}_R \setminus \Lambda^0(\hat{F}_R)$ and can only intersect diagonal edges on $\Lambda^0(\hat{F}_R)$;*
- (iii) *all the curves in $C_f(\hat{F}_R)$ are strictly increasing with respect to the coordinates $(\hat{\xi}_1, \hat{\xi}_2)$ (or all strictly decreasing).*

Proof. First, we note that AA critical points do not change by refinement. The curves are smooth since they are the intersection of a smooth surface (image of a polynomial map) with a plane.

Let us prove (i) by contradiction. We assume that some $\hat{\gamma}_f^0, f \in \Lambda^2(K)$ is tangent to a $\hat{\xi}_1$ -aligned AA line on $\hat{F}_R \setminus \Lambda^0(\hat{F})$. The point was a $\hat{\xi}_1$ -critical point before the refinement. As a result, after refinement, this point belongs to a $\hat{\xi}_2$ -aligned axis of \hat{F}_R (by (1) in ref_1). Then, the point can only be in $\Lambda^0(\hat{F}_R)$. We proceed analogously for $\hat{\xi}_2$ -aligned lines.

Next, we prove (ii). By definition of the refinement rule, there cannot be AA critical points in \hat{F}_R° . We also know that the curves cannot be tangent to AA sides. Thus, by the implicit function theorem, $\hat{\gamma}_f(\hat{\xi}) = 0$ can be expressed as the graph of a function $d_1(\hat{\xi}_1) = \hat{\xi}_2$ and $d_2(\hat{\xi}_2) = \hat{\xi}_1$ in $\hat{F} \setminus \Lambda^0(\hat{F})$. Since these functions are smooth, by the mean value theorem, they must be strictly monotonic in \hat{F} with respect to $\hat{\xi}_1$ and $\hat{\xi}_2$. Thus, they can intersect AA lines at most once. Besides, all intersections against diagonal sides are on $\Lambda^0(\hat{F}_R)$ after refinement (by (2) in ref_1); note that we are not inserting new non-AA edges by refinement.

Finally, we prove (iii). We note that the partition in step (3) or ref_1 prevents two curves $\hat{\alpha}_f, \hat{\alpha}'_f \in C_f(\hat{F}_R)$, strictly increasing and decreasing, resp., to be in the same \hat{F}_R . Let us assume that these two curves are in \hat{F}_R before step (3). Then, by refining through the intersection points of $\hat{\alpha}_f$, we create the axis-aligned bounding box (AABB) of the curve; an AABB is the smallest axis-aligned hypercube that contains a given entity (see, e.g., [56]). $\hat{\alpha}_f$ (which cannot touch the face boundary as proven above) splits the face into two parts, including the bottom-left and top-right vertices of this face, resp. A strictly decreasing curve in this face must connect the left-top and bottom-right edges intersecting $\hat{\alpha}_f$. However, this is not possible since $\hat{\alpha}_f$ and $\hat{\alpha}'_f$ are disconnected components of a non-self-intersecting curve $\hat{\gamma}_f^0$ (since ϕ_F is a diffeomorphism). \square

Proposition 3.5. *Given $f, f' \in \Lambda^2(K)$, $f \neq f'$, and connected components $\hat{\alpha}_f \in C_f(\hat{F}_R)$ and $\hat{\alpha}_{f'} \in C_{f'}$, satisfy the following properties in $\hat{F}_R \in \text{ref}_1(\hat{F})$,*

- (i) $\hat{\alpha}_f$ intersects at most once an edge $\hat{e} \in \Lambda^1(\hat{F}_R)$ and is not tangent to the edge;
- (ii) if $\hat{\alpha}_f$ intersects \hat{F}_R° , $\hat{\alpha}_f$ intersects twice $\partial\hat{F}_R$;
- (iii) $\hat{\alpha}_f$ and $\hat{\alpha}_{f'}$ do not intersect in $\overline{\hat{F}_R} \setminus \Lambda^0(\hat{F}_R)$;
- (iv) $\hat{\alpha}_f$ and $\alpha_{f'}$ intersects at most once in $\overline{\hat{F}_R}$.

Proof. Statement (i) is a direct consequence of Prop. 3.4. Let us prove (ii) by contradiction. We assume that there exists a $\hat{\alpha}_f \in C_f(\hat{F}_R)$, $f \in \Lambda^2(K)$, that does not intersect any edge $\hat{e} \in \Lambda^1(\hat{F}_R)$. $\hat{\alpha}_f$ is a closed curve in \mathbb{R}^2 . This curve is not monotonic, which is in contradiction with Prop. 3.4. If we assume that $\hat{\alpha}_f \in C_f(\hat{F}_R)$, $f \in \Lambda^2(K)$ intersects only once $\partial\hat{F}_R$, then $\hat{\alpha}_f$ is tangent to an edge $\hat{e} \in \Lambda^1(\hat{F}_R)$, which is in contradiction with (i). $\hat{\alpha}_f$ cannot intersect more than twice $\partial\hat{F}_R$ since $\hat{\alpha}_f$ is a connected and non-self-intersecting curve.

All intersections are on vertices of refined faces by step (2) in ref_1 , which proves (iii). Step (3) in the refinement rule explicitly enforces (iv). □

We note that we have not provided yet an algorithm that determines $C_f(\hat{F}_R)$, $f \in \Lambda^1(\hat{F}_R)$, i.e., the $\hat{\alpha}$ -curves after ref_1 . We can compute all the intersections (vertices) but it still remains open how to connect these vertices. We develop the details of the connectivity of the intersection points in the next section. In any case, assuming that the $\hat{\alpha}$ -curves are connected, we can define the following refinement rule ref_2 to compute the intersection $\hat{F}_R \cap K$, where $\hat{F}_R \in \text{ref}_1(\hat{F})$. The ref_2 is not AA but it does not introduce new intersection points, as stated in Th. 3.6 (see Fig. 5).

Algorithm 2 ref_2 : partition by connecting intersections

Split $\hat{F}_R \in \text{ref}_1(\hat{F})$ through each edge $\alpha \in C_f(\hat{F}_R)$, $\forall f \in \Lambda^2(K)$.

Theorem 3.6. *The previous refinement rule is such that $\hat{F}_R \in \text{ref}_2 \circ \text{ref}_1(\hat{F})$ has the following properties:*

- (i) $\Lambda^1(\hat{F}_R)$ is composed of AA edges and strictly monotonic nonlinear edges (including potential diagonal edges);
- (ii) The vertices of \hat{F}_R lay on the boundary of its AABB;
- (iii) All the nonlinear edges are strictly increasing or all strictly decreasing;
- (iv) \hat{F}_R is diffeomorphically equivalent to a convex linear polygon P^{ln} ;

Proof. We note that the refinement ref_1 is a kd -tree partition of the square that contains the reference triangle. Let us consider the set of AABBs obtained by this refinement. By construction of the partition, $\hat{F}_R \in \text{ref}_2 \circ \text{ref}_1(\hat{F})$ is the clipping of an AABB by strictly monotonic curves that do not intersect among themselves (see Prop. 3.4 (ii) and Prop. 3.5). Thus, (i) and (ii) readily hold, while (iii) holds due to Prop. 3.4 (iii).

The nonlinear polygon can be represented as a cyclic graph, where the vertices are the intersection points of the edges. We can replace the nonlinear edges with linear ones connecting the vertices, creating a closed linear polygon. Since the nonlinear edges are smooth, the vertices are preserved, and the topology of the surface is preserved, the linear polygon is diffeomorphic to the nonlinear one. Thus, (iv) holds. □

After refining F , the $\hat{\gamma}^0$ -curves do not intersect \hat{F}_R° , i.e., they belong to $\partial\hat{F}_R$, for $\hat{F}_R \in \text{ref}_2 \circ \text{ref}_1(\hat{F})$. Thus, \hat{F}_R° can only be inside or outside K . Now, we can classify the faces with respect to K as interior,

$$\mathcal{F}^{\text{cut}} \doteq \{ \hat{F}_R \in \text{ref}_2 \circ \text{ref}_1(\hat{F}) : \hat{F}_R \subseteq \bigcap_{f \in \Lambda^2(K)} \text{int}(\hat{\gamma}_f) \}, \quad (9)$$

and exterior, $\mathcal{F}^{\text{ext}} \doteq \{ \hat{F}_R \in \text{ref}_2 \circ \text{ref}_1(\hat{F}) \} \setminus \mathcal{F}^{\text{cut}}$. Remember that K is not open or closed in general, as stated at the beginning of this section. Thus, $\text{int}(\hat{\gamma}_f)$ (where $\text{int}(\cdot)$ denotes the interior), $f \in \Lambda^2(K)$ in (9) can be either open or closed (see more details in [4]). Once the refined faces are classified, we define Alg. 3 to obtain $F \cap K$ as a partition into nonlinear polygons (see Fig. 5). We note that, due to Th. 3.6,

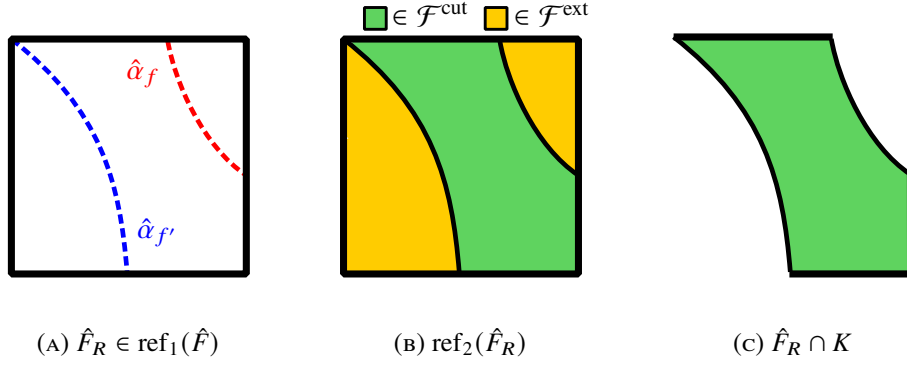


FIGURE 5. Representation of clipping algorithm $F \cap K$. In (a), we start with a refined face $\hat{F}_R \in \text{ref}_1(\hat{F})$ such that the $\hat{\alpha}$ -curves are strictly monotonic with respect to the axes in the reference space and do not intersect in $\hat{F}_R \setminus \Lambda^0(\hat{F}_R)$. Here, the $\hat{\alpha}$ -curves are $\hat{\alpha}_f \in C_f(\hat{F}_R)$ (red) and $\hat{\alpha}_{f'} \in C_{f'}(\hat{F}_R)$ (blue) for $f, f' \in \Lambda^2(K)$. Then, in (b), we generate a partition $\text{ref}_2(\hat{F}_R)$ through the $\hat{\alpha}$ -curves, in which we classify the faces with respect to K . Finally, in (c), we restrict $\text{ref}_2(\hat{F}_R)$ inside K (see Alg. 2).

the linearization of \mathcal{F}^{ref} can be represented with a cyclic graph (see [4]). Thus, \mathcal{F}^{cut} can utilize such representation.

Algorithm 3 $F \cap K$

Compute the partition $\mathcal{F}^{\text{ref}} \doteq \text{ref}_2 \circ \text{ref}_1(F)$.

Return the faces \mathcal{F}^{cut} in \mathcal{F}^{ref} that are inside K (see (9)).

Remark 3.7. For linear F and intersection curves, the AA critical point computation is ill-posed. However, there is no need to add any point in this case, since the intersection is linear. The curve-plane intersection is ill-posed if the curve is contained in the plane (linear edge); analogously for the surface-line intersection (linear face). These intersections can also be disregarded because they are not affecting the meas_2 of sets after trimming.

Remark 3.8. The partition generated by the refinement above may contain a level of refinement that is not required to fulfill all the requirements for Prop. 3.5 to hold. Thus, one can perform a coarsening step of \mathcal{F}^{ref} that reduces the non-essential vertices, edges, and faces, while maintaining a diffeomorphically equivalent surface.

Remark 3.9. The presence of AA critical points can improve the accuracy of a parametrization step in Sec. 3.5, since the resulting curves are strictly monotonic with respect to the edges of the reference space. Additionally, one can consider another refinement of the γ_f^0 -curves to bound the relative chord $\hat{\delta}_{\max}$ up to a given threshold.

3.3. Connection algorithm. Let us consider a face $F \in \text{ref}_1(F^0)$ after the refinement in Alg. 1. We stress that F hereafter denotes a refined face and F^0 the original face before refinement in the previous section. We remark that the reference space is always the one of the original face, i.e., the map ϕ_F is inherited from the unrefined face. Thus, the curves γ_f^0 are independent of the refinement.

As above, let us consider the set $C_f(\hat{F})$ of mutually disconnected components of $\hat{\gamma}_f^0 \cap \bar{\hat{F}}$ (now at the refined face). We omit the face sub-index, i.e., we use $C(\hat{F})$, to represent the union of all these sets for all faces $f \in \Lambda^2(K)$. In the reference space \hat{F} , the curves $\hat{\alpha}_f \in C_f(\hat{F})$ are strictly monotonic smooth curves in $\hat{F} \setminus \Lambda^0(\hat{F})$ (see Prop. 3.4); for brevity, we refer as monotonic the curves that are monotonic with respect to $(\hat{\xi}_1, \hat{\xi}_2)$. In Prop. 3.4, we prove that all the curves in $C_f(\hat{F})$ are strictly increasing or all curves are strictly decreasing. Moreover, two $\hat{\alpha}$ -curves, $\hat{\alpha}_f \in C_f(\hat{F})$ and $\hat{\alpha}_{f'} \in C_{f'}(\hat{F})$, $f, f' \in \Lambda^2(K)$, cannot intersect in $\hat{F} \setminus \Lambda^0(\hat{F})$ (see Prop. 3.5). Let us define the set of intersection points:

$$I = \{\hat{\gamma}_f^0 \cap \partial \hat{F} : f \in \Lambda^2(K)\}.$$

There is an injective map between the intersection points in I and the α -curves. We assume that I is composed of isolated points, i.e., $\hat{\gamma}_f^0 \cap \partial\hat{F}$ is not an edge of \hat{F} . This singular case can readily handled, as discussed in Rmk. 3.7.

By construction (clipping of the reference triangle with AA lines), \hat{F} has four edges and the bottom-left corner connects two AA edges. Thus, we can label the edges of $\Lambda^1(\hat{F})$ as $\hat{\varepsilon}_1, \dots, \hat{\varepsilon}_4$ in the counterclockwise direction, starting with the leftmost vertical edge. We note that $\hat{\varepsilon}_3$ can be non-AA and $\hat{\varepsilon}_4$ empty, but it does not affect the discussion. The refinement rules ensure that the non-AA edges are not intersected by $\hat{\gamma}_f^0$. One can simply consider the AABBB that contains the face, which cannot affect the intersection points, since the $\hat{\alpha}$ -curves only connect AA edges that do not change by this step. Thus, we can assume that all edges are AA without loss of generality.

Let us consider $C_f(\hat{F})$ to be composed of strictly increasing curves. We define $\Gamma^+ \doteq \hat{\varepsilon}_1 \cup \hat{\varepsilon}_2$ and $\Gamma^- \doteq \partial\hat{F} \setminus \Gamma^+$ and $I^+ \doteq I \cap \Gamma^+$ and $I^- \doteq I \cap \Gamma^-$. We proceed analogously if $C_f(\hat{F})$ is composed of strictly decreasing curves, but defining $\Gamma^+ \doteq \hat{\varepsilon}_1 \cup \hat{\varepsilon}_4$.

Proposition 3.10. *Every node in I^+ is connected to one and only one node in I^- . The opposite is also true. Thus, we can connect all the nodes in I^+ and I^- .*

Proof. Let us consider the case in which $C_f(\hat{F})$ is composed of strictly increasing curves. A node in I^+ cannot be connected to a node in I^+ since one node in I belongs to only one curve, the curves are strictly increasing, and a strictly increasing function that starts in ε_1 or ε_2 cannot intersect again ε_1 or ε_2 . Using an analogous argument, we can prove the result when $C_f(\hat{F})$ is composed of strictly decreasing curves. \square

Proposition 3.11. *If I^+ and I^- are sorted clockwise and anti-clockwise, resp., then each node in I^+ can only be connected to the node in the same position in I^- .*

Proof. Let us assume that $i_1^+ \in I^+$ is connected to $i_k^-, k \neq 1$. The line that connects i_1^+ and i_k^- split \hat{F} into two non-empty parts. We note that this is due to the fact that i_1^+ and i_k^+ cannot be on the same edge. One of the parts contains nodes $i_1^-, \dots, i_{k-1}^- \in I^-$ and the other part contains $I^+ \setminus i_1^+$. By Prop. 3.10, nodes contained in the two different regions are connected by α -curves. But these α -curves then intersect the one connecting i_1^+ and i_k^- . This is not possible, since these are disconnected components of a non-self-intersecting curve. Thus, i_1^+ can only be connected to i_1^- . We proceed analogously for the other nodes. \square

This way, we compute all the connections in the graph with Alg. 4. First, in line 1, we compute the intersections between $\hat{\gamma}_f^0$ and $\partial\hat{F}$ using intersection algorithms (see Fig. 6a). In line 3, we return the straightforward connection of two points. Otherwise, in line 5, we compute the derivative sign of the α -curves in $C_f(\hat{F})$ (e.g., evaluating the gradient $\nabla(\hat{\gamma}_f^0)$ at any intersection point $i \in I$). Next, we connect¹ the nodes in the sorted sets I^+ and I^- according to Prop. 3.11 (line 6-8). The algorithm returns a set of edges \mathcal{E} that connect the intersections I . These connections define entirely the $\hat{\alpha}$ -curves, which are then used in Alg. 2. We note that the full connection algorithm is barely used in practice if we start with a surface mesh with a small chordal error of its linearisation.

Algorithm 4 connect($\hat{F}, \hat{\gamma}_f$)

```

1:  $I \leftarrow \{\hat{\gamma}_f^0 \cap \partial\hat{F}\}$ 
2: if length( $I$ ) = 2 then
3:   return  $\mathcal{E} \leftarrow \{i_1, i_2 \in I\}$ 
4: end if
5:  $s \leftarrow \text{derivative\_sign}(\hat{\gamma}_f^0)$ 
6:  $I^+, I^- \leftarrow \text{split\_by\_position}(I, s)$ 
7:  $I^+, I^- \leftarrow \text{cyclic\_sort\_by\_sign}(I^-, I^+, s)$ 
8: return  $\mathcal{E} \leftarrow \{ (i^+, i^-) \in \text{zip}(I^+, I^-) \}$ 

```

¹In line 8, we use the notation `zip` to iterate simultaneously over multiple iterators of the same length, e.g., \mathbf{a} and \mathbf{b} . Each iteration returns a tuple of the i^{th} value of each iterator, (a_i, b_i) .

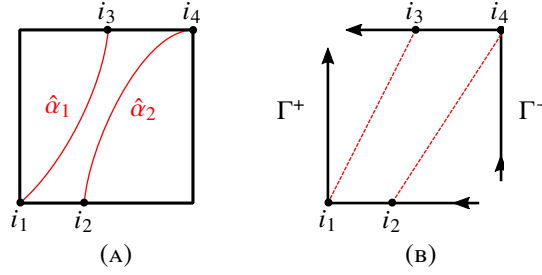


FIGURE 6. Representation of Alg. 4 for strictly increasing curves. In (a), we present the intersections $i_1, \dots, i_4 \in I$ of the curves $\hat{\alpha}_1, \hat{\alpha}_2 \in C_f(\hat{F})$ with $\partial\hat{F}$. These intersections are classified into $I^+ = \{i_3, i_4\}$ and $I^- = \{i_1, i_2\}$ according to their position in the boundary, Γ^+ or Γ^- , resp. These sets are sorted in clockwise and anticlockwise order, resp. This sorting leads to the connection shown in (b) (dashed red). If the curves in $C_f(\hat{F})$ were strictly decreasing, the figures would be symmetric to these ones.

Remark 3.12. In the computation of intersection points in Alg. 4, we disregard the ones that do not logically represent an intersection. E.g., if the level set value γ_f does not change the sign around a vertex with zero level set value.

One can observe that for this algorithm to work, I must have an even number of elements (after filtering I with Rmk. 3.12). It is true since the $\hat{\alpha}$ -curves are monotonic. Thus, any $\hat{\alpha}_f \in C_f(\hat{F})$ that $\hat{\alpha}_f \cap \hat{F} \setminus \Lambda^0(\hat{F}) \neq \emptyset$ can only intersect twice $\partial\hat{F}$ (see Th. 3.6).

3.4. Surface partition. Let us consider a nonlinear general polygon \hat{F} in \mathbb{R}^2 , e.g., $F \in \mathcal{F}^{\text{cut}}$. In order to parametrize F , we need a partition into regular polygons, e.g., simplices or quadrilaterals. This parameterization is needed to compute bulk and surface integrals when using (5). However, this is not needed when transforming these integrals into edge integrals using (6).

Let us recover the definition of a kernel point. A kernel point can be connected by a segment to any other point of a polytope without intersecting its boundary. The union of all possible kernel points is the kernel polytope, which is convex. The kernel polytope of a convex polytope is itself [57]. In a linear polytope P^{ln} , we can compute a kernel point by finding a point that belongs to the half-spaces defined by the faces of P^{ln} ; see more details in [58].

Finding the kernel of a nonlinear polytope \hat{F} is not trivial. One can find a lower bound of the kernel polytope with the convex hull of the nonlinear faces. If a kernel point exists for a given polytope \hat{F} , we can compute a simplex partition of \hat{F} using linear edges. However, the kernel point does not exist in general.

Proposition 3.13. If \hat{F} has the properties of Th. 3.6 then \hat{F} can be partitioned into a set of nonlinear triangles and quadrilaterals by adding linear edges only.

Proof. Let us assume that $\Lambda^1(\hat{F})$ is composed of two strictly increasing nonlinear curves and a set of AA edges. According to Th. 3.6, these curves and edges can only intersect at the boundary of the AABB of \hat{F} . Thus, we connect the endpoints of the nonlinear curves with non-increasing linear edges. Since the new edges are non-increasing, they can only intersect once each curve, i.e., at the endpoints. This connection generates a nonlinear quadrilateral $\hat{Q} \subseteq \hat{F}$. The remaining parts $\hat{F} \setminus \hat{Q}$ are linear and convex (see Th. 3.6), in which a simplex partition is straightforward. \square

Therefore, we can compute a hybrid partition if a nonlinear polytope \hat{F} has no kernel point. We note that the nonlinear quadrilaterals of Prop. 3.13 are composed of two nonlinear edges and two linear edges. Thus, they can be represented with a tensor product map with anisotropic order, e.g., $q \times 1$ where q is the order of the nonlinear edges. If needed, we can decompose the nonlinear quadrilaterals into triangles within their reference space.

Remark 3.14. We can consider a coarsening of \mathcal{F}^{cut} that satisfies Prop. 3.5 (see Rmk. 3.8) if the resulting polygons have a kernel point. We note that the coarsening stated in Rmk. 3.8 can lead to non-convex polygons.

3.5. Surface parametrization. The intersection $\mathcal{B}_K^{\text{cut}} \doteq \mathcal{B} \cap K$ is a nonlinear surface mesh in which the intersection curves are implicitly represented. Thus, we need a parametrization of the edges and surfaces for further operations. We utilize a least-squares method [49] combined with a sampling strategy [5]. This iterative process converges to an accurate parametrization of the intersection curves and trimmed surfaces.

In the least-squares method we can find the Bézier control points $X^b = \{x_j^b\}_{j=1}^m$ that minimize $X^\ell - \mathbf{B}X^b$ where $\{\mathbf{B}\}_{ij} = b_j(\xi_i)$ are the Bézier basis evaluated at the reference points $\{\xi_j\}_{j=1}^n$ and $X^\ell = \{x_j^\ell\}_{j=1}^n$ represents the set of sampling points (see [59] for more details). When \mathbf{B} is not a square matrix, i.e., $n > m$, X^b is approximated through a linear least-squares operation. To isolate the approximation between the d -faces, one can recursively perform a least-squares operation on the interior points, increasing the dimension. Note that for square matrices, i.e., $n = m$, we are building the Bézier extraction operator [45].

Fries and Omerović [5] discussed several sampling strategies and demonstrated similar convergence in FE analysis. In each of the sampling strategies, they solve a nonlinear problem for every sampling point. In our case, we aim to parametrize the intersection curves $F \cap G$, $F \in \mathcal{B}$, $G \in \Lambda^2(K)$. Thus, we define a sampling strategy to represent the intersection curves by solving a closest point problem. Specifically, we find

$$\hat{\xi} \in \hat{F} : (x_0 - \phi_F(\hat{\xi})) \cdot n_\pi = 0, \quad (x_0 - \phi_F(\hat{\xi})) \cdot (n_\pi \times (\partial_{\hat{\xi}_1}(\phi_F(\hat{\xi})) \times \partial_{\hat{\xi}_2}(\phi_F(\hat{\xi})))) = 0.$$

When we compute the closest point to a surface, e.g., when parametrizing the interior of a nonlinear face, the problem reads as follows: find

$$\hat{\xi} \in \hat{F} : (x_0 - \phi_F(\hat{\xi})) \cdot \nabla(\phi_F(\hat{\xi})) = 0.$$

This algorithm requires a seed point in the physical space x_0 , which does not belong to the surface or curve, and an initial reference point $\hat{\xi}_0 \in \hat{F}$. This sampling strategy, as well as others, assumes relatively small curvature in the curves and surfaces. The curvature has already been bounded in Sec. 3.2.

The least-squares method with a sampling strategy is insufficient for an accurate parametrization, see the example of Fig. 7b. The authors in [49] propose a method to optimize the reference points $\{\xi_j\}_{j=1}^n$ iteratively. We use a similar approach that fixes the reference points and recomputes the sampling points at each iteration. This approach allows us to compute the least-squares operator \mathbf{B}^+ only once. In addition, the sampling will be evenly spaced in the reference space. The example in Fig. 7 shows how the approximation improves with the iterations. This method applies to the parametrization of curves and surfaces.

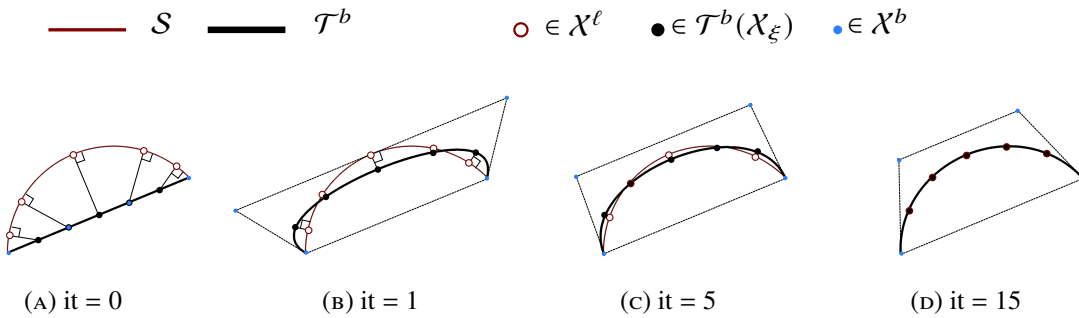


FIGURE 7. Example of iterative approximation of a curve. From the linear approximation in (a), we sample the closest points. These sampling points X^ℓ are approximated in a Bézier curve X^b in (b). In (b), we evaluate the approximated seed points $\mathcal{T}^b(X_\xi)$ to compute the new sampling points. Across the iteration, in (c) and (d), the approximation improves by reducing the distance between the sampling points and the curve. In (d), the sampling points are evenly spaced in the reference space (up to a stopping criterion). Note that this example corresponds to a particular case of the Alg. 5 in which the approximation degree is fixed to $p = 3$.

The parameterization method is described in Alg. 5. Even though this algorithm is designed for $\mathcal{B}_K^{\text{cut}}$, it is general to any nonlinear mesh, namely \mathcal{S} . We first generate a linear approximation of \mathcal{S} in line 1 with a simplex partition (or a partition into standard polytopes, see Sec. 3.4). In line 2, we initialize the sampling

points through the degree elevation, see [26]. Then, we parametrize the d -faces from lower to higher dimension line 3. Each d is parametrized from lower to higher order line 4, in simplices, we start with $p^0 = d$. The gradual increment of the approximation error improves the convergence. In each iteration, we compute a Bézier mesh with the least-squares method then we compute the sampling points from the evaluations of the Bézier mesh. When the variation of the error estimator is below a tolerance, we increase the degree. Finally, we return the Bézier mesh with the least-squares method of the highest degree.

Algorithm 5 $\text{parametrize}(\mathcal{T}, D)$

```

1:  $\mathcal{T}^{\text{lin}} \leftarrow \text{simplexify}(\mathcal{S}, D)$ 
2:  $\mathcal{T}^\ell \leftarrow \text{elevation}(\mathcal{T}^{\text{lin}}, p^\ell)$ 
3: for  $d \in \{1, \dots, D\}$  do
4:   for  $p \in \{p^0, \dots, p^b\}$  do
5:      $e^- \leftarrow \infty$ ;  $\Delta e \leftarrow \infty$ 
6:     while  $\Delta e > \epsilon$  do
7:        $\mathcal{T}^b \leftarrow \mathbf{B}_p^+ \cdot \mathcal{T}_d^\ell$ 
8:        $\mathcal{T}_d^\ell \leftarrow \text{sample}(\mathcal{T}^b, \mathcal{T}_d^\ell, \mathcal{S})$ 
9:        $e \leftarrow \|\mathcal{T}^b - \mathcal{T}_d^\ell\|_{\ell^2}$ ;  $\Delta e \leftarrow |e - e^-|/e$ ;  $e^- \leftarrow e$ 
10:    end while
11:  end for
12: end for
13: return  $\mathbf{B}_{p^b}^+ \cdot \mathcal{T}^\ell$ 

```

3.6. Cell intersection. The intersection of a cell with the domain $K^{\text{cut}} \doteq K \cap \Omega$ can be represented using its boundary $\partial K^{\text{cut}} \doteq (\partial K)^{\text{cut}} \cup \mathcal{B}_K^{\text{cut}}$, as stated in Sec. 2.2. In Alg. 6, we aim to compute $(\partial K)^{\text{cut}} \doteq \partial K \cap \Omega = \partial K \cap \text{int}(\mathcal{B}_K^{\text{cut}})$ using the linear algorithms from [4]. Here, $\text{int}(\mathcal{B}_K^{\text{cut}})$ represents the domain bounded by $\mathcal{B}_K^{\text{cut}}$. For this purpose, we first need a linearized surface $\mathcal{B}_K^{\text{lin}} \doteq \text{lin}(\mathcal{B}_K^{\text{cut}})$ partitioned into simplices (see line 1 and Fig. 8a to Fig. 8b). Since $\mathcal{B}_K^{\text{cut}}$ is composed of nonlinear polytopes that are diffeomorphically equivalent to linear and convex polytopes, both linearization and simplex decomposition are straightforward.

The main algorithm in [4] provides a linearized partition for K^{cut} , i.e., $\mathcal{T}_K^{\text{lin}} \doteq K \cap \mathcal{B}_K^{\text{lin}}$ in line 2 and Fig. 8c. From $\mathcal{T}_K^{\text{lin}}$, we can obtain $(\partial K)^{\text{lin}}$ by filtering the faces that belong to ∂K in line 3. Additionally, we merge cells $P \in (\partial K)^{\text{lin}}$ such that $\Lambda^1(P)$ is composed of cell edges $\varepsilon_K \subseteq \varepsilon \in \Lambda^1(K)$ and surface edges $\varepsilon_{\mathcal{B}} \in \Lambda^1(\mathcal{B}_K^{\text{lin}})$. It is important to note that the surface edges $\varepsilon_{\mathcal{B}} \in \Lambda^1(\mathcal{B}_K^{\text{lin}})$ have bijective map to $\varepsilon'_{\mathcal{B}} \in \Lambda^1(\mathcal{B}_K^{\text{cut}})$, namely $\Phi_{\mathcal{B}} : \varepsilon_{\mathcal{B}} \mapsto \varepsilon'_{\mathcal{B}}$. Therefore, we recover the nonlinear cell boundary intersection $(\partial K)^{\text{cut}}$ by replacing the $\varepsilon_{\mathcal{B}}$ edges with the ones parametrized in $\mathcal{B}_K^{\text{cut}}$ (see line 4 and Fig. 8d).

Algorithm 6 $\partial K \cap \text{int}(\mathcal{B}_K^{\text{cut}}) \rightarrow (\partial K)^{\text{cut}}$

```

1:  $\mathcal{B}_K^{\text{lin}} \leftarrow \text{lin}(\mathcal{B}_K^{\text{cut}})$ 
2:  $\mathcal{T}_K^{\text{lin}} \leftarrow K \cap \text{int}(\mathcal{B}_K^{\text{lin}})$ 
3:  $(\partial K)^{\text{lin}} \leftarrow \{F \in \Lambda^2(P) : P \in \mathcal{T}_K^{\text{lin}}, F \subset \partial K\}$ 
4: return  $(\partial K)^{\text{cut}} \leftarrow \text{replace\_edges}((\partial K)^{\text{lin}}, \Phi_{\mathcal{B}})$ 

```

The parametrization of the edges of $(\partial K)^{\text{cut}}$ is extracted from $\mathcal{B}_K^{\text{cut}}$. However, the surface parametrization requires a surface partition into standard polytopes. We utilize the methods described in Sec. 3.4 to build such a partition. In this case, the AA critical points and AA partitions are defined in the reference space of $P \in (\partial K)^{\text{cut}}$, i.e., in the reference space of $F \in \Lambda^2(K)$. It is worth noting that, in this partition, the intersections of the nonlinear edges $\varepsilon \in \Lambda^1(\mathcal{B}_K^{\text{cut}})$ with AA lines are computed in the reference space of ε . This fact ensures local conformity.

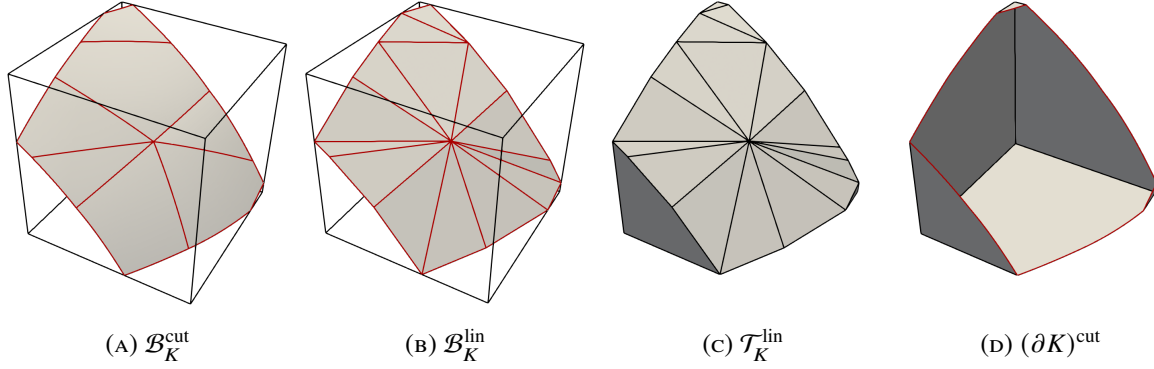


FIGURE 8. Representation of the steps that generate $(\partial K)^{\text{cut}}$. First, the surface portion $\mathcal{B}_K^{\text{cut}}$ (see (a)) is linearized and partitioned into simplices ($\mathcal{B}_K^{\text{lin}}$ in (b)). Then, in (c), we intersect the background cell K with the half-spaces of the planes of \mathcal{B}^{lin} using linear algorithms, resulting in $\mathcal{T}_K^{\text{lin}}$. This linear intersection is possible since the faces $F \in \mathcal{B}_K^{\text{lin}}$ are planar. Next, we extract the boundary of $\mathcal{T}_K^{\text{lin}}$ that belong to ∂K , leading to $(\partial K)^{\text{lin}}$. Finally, we replace the edges in $(\partial K)^{\text{lin}}$ by the ones in $\mathcal{B}_K^{\text{cut}}$ to obtain $(\partial K)^{\text{cut}}$ (see (d)). The boundary of $K \cap \Omega$ is represented by $(\partial K)^{\text{cut}} \cup \mathcal{B}_K^{\text{cut}}$.

3.7. Global algorithm. The algorithms presented in the previous sections are defined cell-wise. In this section, we describe an algorithm that allows us to integrate FE functions in the whole domain and its boundary. Each cell of the background mesh is intersected by the domain bounded by a high-order Bézier surface mesh. Therefore, to proceed, we first need to generate this surface mesh from the given BREP, e.g., analytical functions or CAD representation. From CAD models we can generate high-order surface meshes with a third-party library, e.g., `gms` [53]. We can convert these meshes into Bézier patches with a Bézier projection operation or a least-squares approximation.

The intersection of a background cell $K \in \mathcal{T}$ with the whole surface mesh \mathcal{B} would be inefficient. Therefore, we restrict the surface mesh to the faces colliding with the cell K . We perform this operation in a preprocessing step similar to [4]. The interrogations are approximated by linear operations on the convex hull of each Bézier patch. We can accelerate these queries with a hierarchy of simpler bounding domains, e.g., AABBs, oriented bounding boxes (OBBs) [56] or discrete orientation polytopes (k-DOPs) [60, 61]. We note that these operations prioritize speed over accuracy as the subsequent operations can deal with false positives in the surface restriction.

The global algorithm is described in Alg. 7 and demonstrated through an example in Fig. 9. First, in line 2, the Bézier mesh is extracted from the given representation, e.g., CAD model in Fig. 9a. For each cell $K \in \mathcal{T}$, we restrict the faces $F \in \mathcal{B}$ touching K , see Fig. 9b step (i) and line 4. The surface \mathcal{B}_K is intersected by the walls of K , see step (ii) and line 5. Then, the cell boundary is intersected by the half-spaces of the intersected surface $\mathcal{B}_K^{\text{cut}}$ (line 6). Both boundary intersections $\mathcal{B}_K^{\text{cut}} \cup (\partial K)^{\text{cut}}$ represent the boundary of the cut cell K^{cut} , see step (iii). The parameterization of these is stored for integration purposes (line 7).

Algorithm 7 $\mathcal{T} \cap \text{int}(\mathcal{B}^{\text{CAD}})$

```

1:  $\mathcal{T}^{\text{cut}} \leftarrow \emptyset$ 
2:  $\mathcal{B} \leftarrow \text{extraction}(\mathcal{B}^{\text{CAD}})$ 
3: for  $K \in \mathcal{T}$  do
4:    $\mathcal{B}_K \leftarrow \text{restrict}(\mathcal{B}, K)$ 
5:    $\mathcal{B}_K^{\text{cut}} \leftarrow \mathcal{B}_K \cap K$ 
6:    $(\partial K)^{\text{cut}} \leftarrow \partial K \cap \text{int}(\mathcal{B}_K^{\text{cut}})$ 
7:    $\mathcal{T}^{\text{cut}} \leftarrow \mathcal{T}^{\text{cut}} \cup \text{parametrize}(\mathcal{B}_K^{\text{cut}}) \cup \text{parametrize}((\partial K)^{\text{cut}})$ 
8: end for
9: return  $\mathcal{T}^{\text{cut}}$ 

```

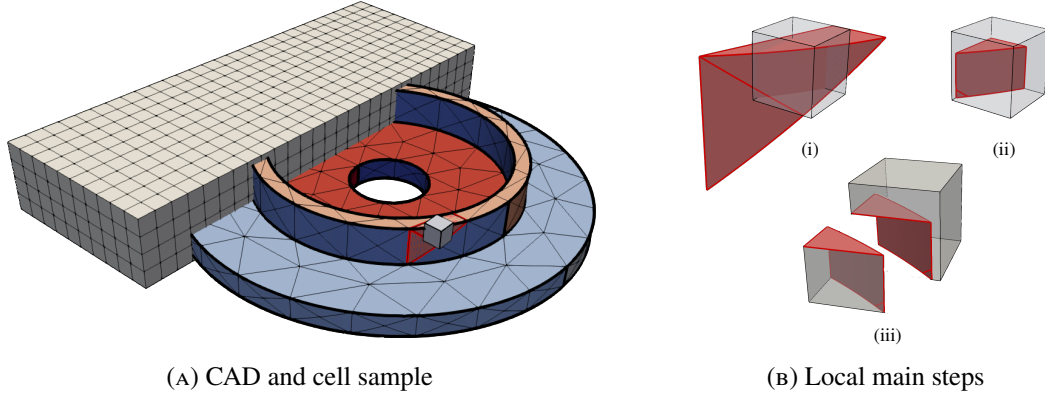


FIGURE 9. In (a) the CAD geometry (colored CAD entities) is first approximated into a high-order surface mesh. In each cell of the background mesh (b), in (i) we restrict the nonlinear faces touching the background cell. Then, in (ii) we clip the nonlinear faces by the background cell walls. Finally, in (iii) we build the polytopal representation of the intersected $\partial K \cap \Omega$. Afterward, we prepare the polytypes for the integration, e.g., with a surface parametrization.

Once we have classified the non-intersected cells as described in [4], we can proceed with the integration over the entire domain. The integration strategy depends on the dimension of the parametrization used in line 7. In the methods described in this section, we utilize high-order 2-faces for parametrization, enabling us to employ Stokes theorem for integration [33] in combination with moment-fitting methods [23]. However, when using edge parametrizations, it is necessary to employ Stokes theorem over trimmed faces [34].

4. NUMERICAL EXPERIMENTS

In the numerical experiments, we aim to demonstrate the robustness of the method and optimal convergence of the geometrical and PDE solution approximations. First, we demonstrate *hp*-convergence of the intersection and parametrization methods in Sec. 4.2. Then, in Sec. 4.3, we show the robustness of the method concerning the relative position of the background mesh and the geometry. Next, in Sec. 4.4, we show the optimal *hp*-convergence of the FE analysis for a manufactured solution of the Poisson equation and an elasticity benchmark. Finally, we show the application of the method in real-world examples on CAD described in terms of standard for the exchange of product model data (STEP) files.

4.1. Experimental setup. The numerical experiments have been performed on Gadi, a high-end supercomputer at the NCI (Canberra, Australia) with 4962 nodes, 3074 of them powered by a 2×24 core Intel Xeon Platinum 8274 (Cascade Lake) at 3.2 GHz and 192 GB RAM. The algorithms presented in this work have been implemented in the Julia programming language [62]. The unfitted FE computations have been performed using the Julia FE library `Gridap.jl` [63, 64] version 0.17.17 and the extension package for unfitted methods `GridapEmbedded.jl` version 0.8.1 [65]. `STLCutters.jl` version 0.1.6 [66] has been used to compute intersection computations on STL geometries. The computations of the convex hulls have been performed with `DirectQhull.jl` version 0.2.0 [67], a Julia wrapper of the `qhull` library [68].

The CAD geometry preprocess is done in `gmsh` library [53] by using the `GridapGmsh.jl` Julia wrapper [69]. The `gmsh` library calls Open CASCADE Technology (OCCT) [70] as a parser for STEP files. The sample geometries are extracted from [70] and [71].

4.2. Approximation and parametrization analysis. In this section, we analyze the approximation of the geometry by a Bézier mesh \mathcal{B} . We use a sphere as test geometry. We define the sphere by the boundary of a reference cube bumped by $f(\hat{\mathbf{x}}) = \mathbf{x}_0 + R(\hat{\mathbf{x}} - \hat{\mathbf{x}}_0)/\|\hat{\mathbf{x}} - \hat{\mathbf{x}}_0\|$ where $\hat{\mathbf{x}}_0$ is the center of the reference cube, \mathbf{x}_0 is the center of the sphere and $R = 1$ is the radius of the sphere in our experiments. In the following experiments, we consider a triangular surface mesh for the reference cube boundary obtained from the convex decomposition of a Cartesian mesh. We define the relative cell size as $h_{\text{surf}} = 1/n_{\text{surf}}$ where n_{surf} is the number of elements in each Cartesian direction. The surface partition of the sphere is approximated

by a Bézier mesh \mathcal{B} of order p by using a least-squares operation. This sphere is embedded in a cube of side $L = 3$. This domain is discretized with a background Cartesian mesh \mathcal{T} of relative cell size $h = 1/n$ where n is the number of cells in each direction. During the intersection of the surface, the relative chord of the edges is bounded to $\hat{\delta}_{\max} < 0.1$. The surfaces are computed by integrating a unit function on the high-order surface mesh, while we use Stokes theorem in the volume computation.

In the surface approximation experiments of Fig. 10a, we test a matrix of surface cell sizes $h_{\text{surf}} = 2^{-\alpha}$, with $\alpha = 2, \dots, 5$ and a range of Bézier orders $p = 1, \dots, 7$. We compute the Bézier approximation error as the difference between the surface of \mathcal{B} and the analytical surface. We observe that the convergence rate of the approximation errors is $p + 1$ for odd orders and $p + 2$ for even orders. In [43], one can observe similar convergence rates of the surface and volume errors. It is worth noting that the convergence rates are affected by machine precision for $p = 6, 7$ in Fig. 10a.

In Fig. 10b, the surface mesh \mathcal{B} is intersecting by each background cell $K \in \mathcal{T}$. This generates \mathcal{B}^{cut} . These intersections are performed for surfaces \mathcal{B} of order p and parametrized with order p , where $p = 2, \dots, 6$. In Fig. 10c, we present the results of intersecting each background cell $K \in \mathcal{T}$ with the domain bounded by \mathcal{B} , resulting in \mathcal{T}^{cut} . In this case, the approximation of \mathcal{B} and surface parametrization are computed with order $p = 2, 3, 4$ for computational reasons. In both cases, the cell size of the background mesh is fixed to $h = 2^{-2}$. We observe in Fig. 10b and Fig. 10c that the convergence rates of the cut surface error, $|\text{surf}(\mathcal{B}^{\text{cut}}) - \text{surf}(\mathcal{B})|$, and the cut volume error, $|\text{vol}(\mathcal{T}^{\text{cut}}) - \text{vol}(\mathcal{B})|$, are similar to the convergence rates of Fig. 10a.

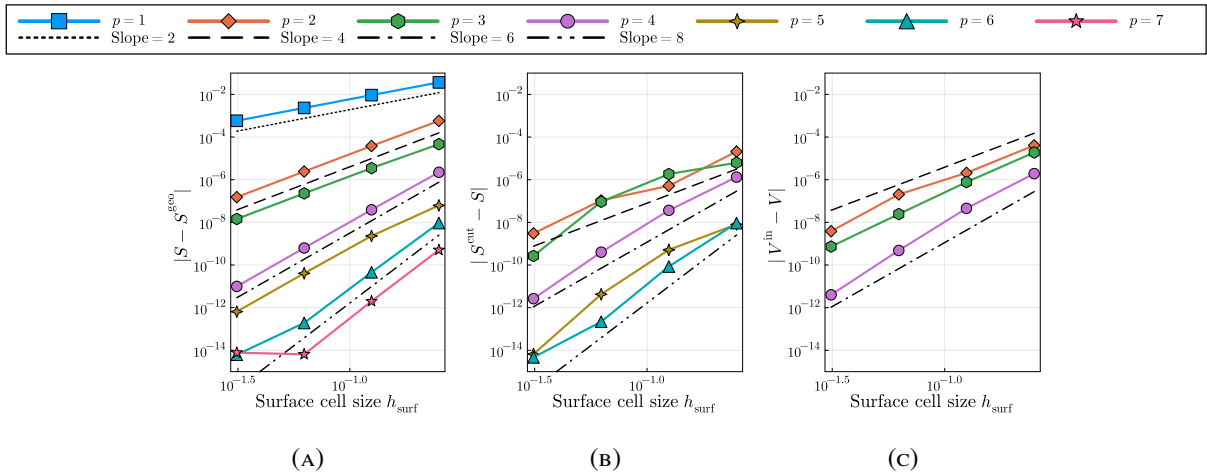


FIGURE 10. Surface and volume errors of the approximation and the reparametrization of a sphere. In (a), the surface error of approximating the geometry \mathcal{B}^{geo} into a Bézier mesh \mathcal{B} , $|S - S^{\text{geo}}|$ where $S^{\text{geo}} = \text{surf}(\mathcal{B}^{\text{geo}})$ and $S = \text{surf}(\mathcal{B})$. In (b), the parametrization error of \mathcal{B}^{cut} , the intersection of \mathcal{B} with each background cell $K \in \mathcal{T}$, $|S^{\text{cut}} - S|$ where $S^{\text{geo}} = \text{surf}(\mathcal{B}^{\text{geo}})$. In (c), the volume integration error of \mathcal{T}^{in} , the intersection of each background cell $K \in \mathcal{T}$ with the domain bounded by \mathcal{B} , $|V^{\text{in}} - V|$ where $V^{\text{in}} = \text{vol}(\mathcal{T}^{\text{in}})$ and $V = \text{vol}(\mathcal{B})$.

4.3. Robustness experiments. In this section, we demonstrate robustness concerning the relative position of \mathcal{B} and \mathcal{T} . For these experiments, we consider a sphere with the same geometrical setup as in Sec. 4.2. We perform the intersections with the same relative background cell size and surface cell size $h = h_{\text{surf}} = 2^{-\alpha}$, $\alpha = 3, 4$. We test for the approximation and parametrization orders $p = 2, \dots, 4$. In each combination, we shift the geometry from the origin a distance $\Delta x = (i/500)h$, with $i = 1, \dots, 500$.

In Fig. 11a and Fig. 11b, we observe the surface and volume variation of the surface error, $|\text{surf}(\mathcal{B}^{\text{cut}}) - \text{surf}(\mathcal{B})|$, and the volume error, $|\text{vol}(\mathcal{T}^{\text{in}}) - \text{vol}(\mathcal{B})|$, resp. Here, $\mathcal{T}^{\text{in}} \doteq \mathcal{T}^{\text{cut}} \cup \{K \in \mathcal{T} : K \cap \partial\Omega = \emptyset\}$ is the physical volume mesh. The variations of the surface error are approximately two orders of magnitude and the variations of volume are one order of magnitude.

However, in Fig. 11c, we observe a machine precision error in the domain volume error $|\text{vol}(\mathcal{T}^{\text{in}}) + \text{vol}(\mathcal{T}^{\text{out}}) - \text{vol}(\mathcal{T}^{\text{bg}})|$, where $\mathcal{T}^{\text{out}} \doteq \mathcal{T}^{\text{bg}} \setminus \mathcal{T}^{\text{in}}$ is complementary of \mathcal{T}^{in} . The low error is due to the conformity between inside and outside polytopes of the cut cell described in Sec. 3.6.

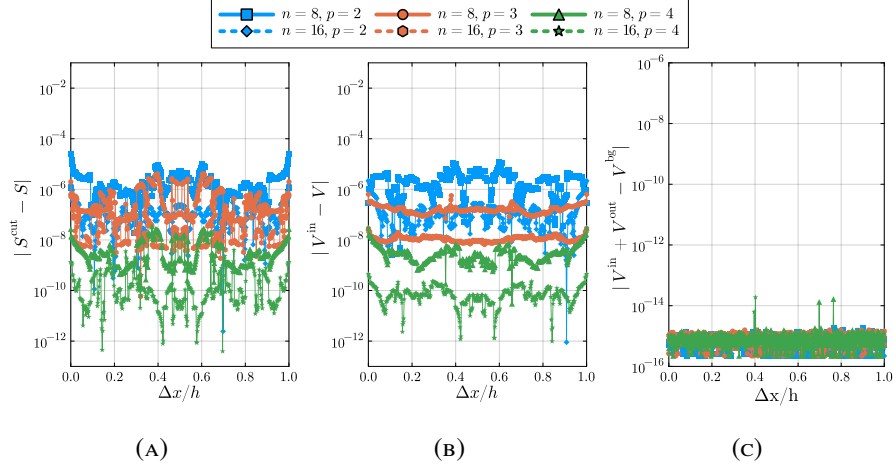


FIGURE 11. Demonstration of robustness concerning the relative position of \mathcal{B} and \mathcal{T} . Both plots have surface and volume errors when shifting a sphere in the embedded domain. Even though the surface and volume errors in (a) and (b) show variations, the errors are bounded. In (c), the domain volume errors are close to machine precision because the inside and outside polytopes of the cut cell are conforming, see Sec. 3.6

4.4. Unfitted FE experiments. In these experiments, we explore the behavior of the intersection algorithms by solving PDEs with unfitted FEs on two analytical benchmarks and two realistic examples. We analyze a Poisson equation with a manufactured solution on a sphere and a spherical cavity benchmark with an analytically derived solution [72]. Both experiments are performed with the geometrical setup described in Sec. 4.2. However, in the spherical cavity experiments, the domain is the outside of an octant of the sphere. We compute the FE solutions using AgFEM with modal C^0 basis and moment-fitting quadratures, even though the proposed framework can be used with other unfitted methods like ghost penalty stabilization [14]. We follow the methodology in [23, Sec. 6.2] for the computation of moment-fitting quadratures; we leverage an extension of Lasserre’s method in [73]. It is shown in [23, Fig. 7] that the computed moment-fitted quadratures are much more efficient than marching cube ones while offering the same level of accuracy (at least) up to $m = 5$. In AgFEM, we aggregate all cut cells.

In the Poisson experiments, we consider Dirichlet boundary conditions and a forcing term that satisfies the manufactured solution $u(x, y, z) = x^a + y^a$, with $a = 6$. We compute the convergence tests for $h = h_{\text{surf}} = 2^{-\alpha}$, with $\alpha = 3, 4, 5$, for the FE order $p = 1, 2, 3$ and the geometrical order $q = 1, 2, 3$ of the approximation and parametrizations. In Fig. 12a and Fig. 12b, we can observe that the L^2 and H^1 errors converge with the optimal rate, $p + 1$ and p , resp. This convergence is independent of the geometrical order q , as expected, the geometry description does not affect the manufactured solution problem.

In the linear elasticity benchmark of the spherical cavity, we derive the potentials with automatic differentiation in Julia. We compute the tests for the same cell sizes $h = h_{\text{surf}} = 2^{-\alpha}$ and orders $p = 1, 2, 3$ and $q = 1, 2, 3$ than in the Poisson experiments. We set consider a Young modulus $E = 10^5$ and Poisson ratio $\nu = 0.3$. We observe in Fig. 12c and Fig. 12d the expected convergence rates for the L^2 and H^1 errors, $\min(p, q) + 1$ and p resp. This demonstrates that we require high-order discretizations to accurately solve PDEs with high-order unfitted FE methods.

Finally, we demonstrate the viability of the method in real-world geometries defined by CAD models in STEP files. These files are extracted from [70] and [71], resp. On each CAD geometry, we generated a high-order surface mesh using gmsh. Then, we converted this mesh into a Bézier mesh with a least-squares method. The indexing of topological entities of the CAD surface, \mathcal{B}^{CAD} , is preserved in the intersected mesh \mathcal{B}^{cut} . Thus, we can impose Dirichlet and Neumann boundary conditions over the entities in \mathcal{B}^{CAD} . We consider a heat problem and an elasticity problem in the two different geometries Fig. 13. The experiments are described in the figure caption.

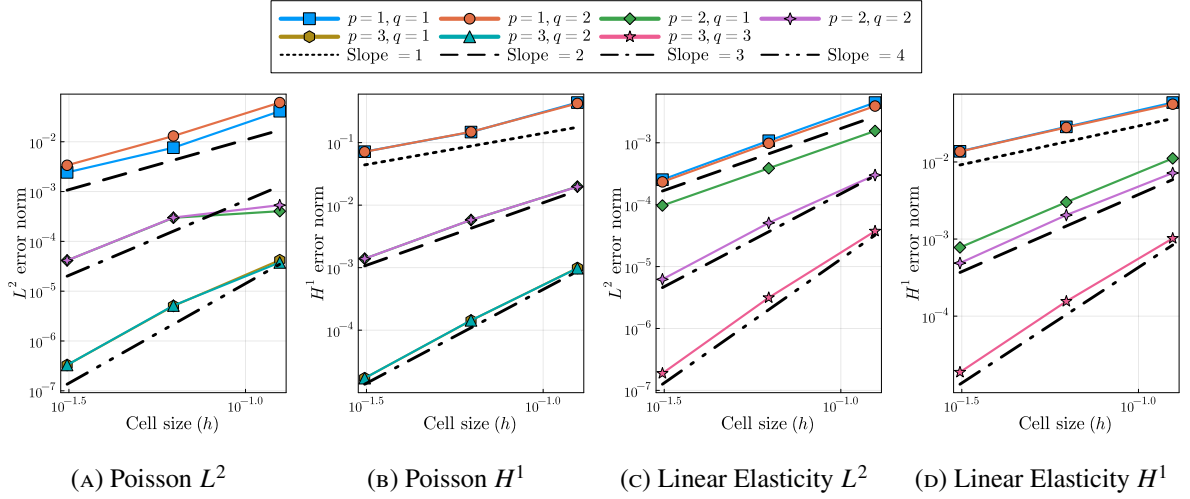


FIGURE 12. Convergence tests in AgFEM. Convergence of the manufactured solution with a Poisson equation in a sphere, in (a) and (b). Convergence of the linear elasticity benchmark in a spherical cavity, in (c) and (d). Some combinations of FE order p and geometry order q are not shown for the sake of conciseness.

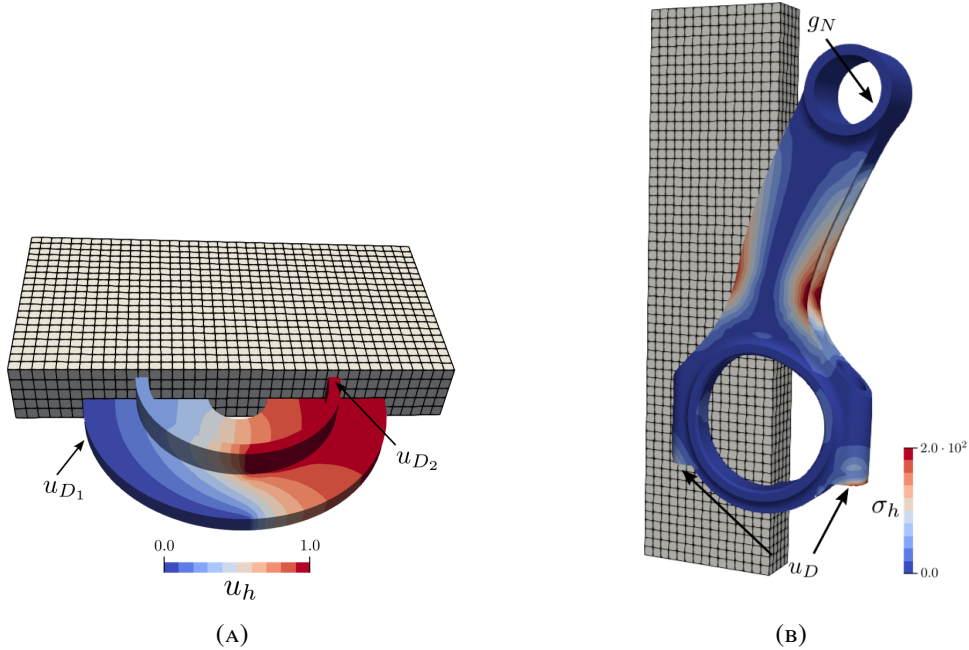


FIGURE 13. Realistic examples on CAD geometries. In (a) we consider a heat equation with thermal conductivity $k = 1.0$ and Dirichlet boundary conditions on two opposite entities ($u_{D_1} = 0$ and $u_{D_2} = 1$). The background mesh is defined in a AABB 20% larger than the geometry with $40 \times 40 \times 5$ elements of order $p = 2$. The surface is approximated in 524 quadratic Bézier patches. In (b) we consider a linear elasticity problem with Young modulus $E = 10^5$ and Poisson ratio $\nu = 0.3$, with Dirichlet and Neumann boundary conditions ($u_D = (0, 0, 0)$ and $g_N = (1, 0, -1)$, resp.). The magnification factor of the deformation is 75. The background mesh is defined in an AABB 20% bigger than the geometry with $30 \times 10 \times 60$ elements of order $p = 2$. The surface is approximated in 1786 quadratic Bézier patches.

5. CONCLUSIONS AND FUTURE WORK

In this work, we have designed an automated pipeline for numerically approximating PDEs in complex domains defined by high-order boundary meshes using unfitted FE formulations in a structured background mesh. The main challenge of the method lies in the numerical integration of the background cells intersected by the domain boundary. This requires handling the intersection between background cells and complex boundary meshes, including the computation of trimming curves and dealing with nonlinear and nonconvex domains.

We have presented a novel intersection algorithm for general high-order surfaces and polytopal cells, which is accurate and robust. The algorithm is based on mesh partition methods for nonlinear level sets, linear clipping algorithms for general polytopes, multivariate root finding, geometrical least-squares methods and the properties of Bézier patches. The result of this algorithm is a set of nonlinear general polyhedra that represent the cut cells of the background mesh. We parametrize the boundary of these polyhedra using sets of Bézier patches, taking advantage of concepts like convex hull and kernel point concepts. These Bézier patches can be used to integrate the bulk with moment-fitting quadratures.

The implementation, accuracy and robustness of the geometrical algorithm have been tested on high-order geometries defined by analytical methods and CAD models. In our tests, we observe optimal convergence of the numerical approximations, limited only by rounding errors. Additionally, we have observed the robustness of the method when varying the relative position of the background mesh. Furthermore, we have successfully solved PDEs on geometries defined by nonlinear boundary representations with high-order FE methods. We have demonstrated optimal convergence of the solutions in the designed benchmarks. We have also shown the viability of the method in real-world geometries defined by CAD models in STEP files. These results position the method as a pioneering computational framework for simulating PDEs on high-order geometries with unfitted FE methods. It provides an automatic geometrical and functional discretization that can be especially useful within shape and topology optimization loops, inverse problems with unknown boundaries and interfaces, and transient problems with moving domains.

Future work involves the extension of the method for other background discretizations, e.g., octree meshes for adaptive refinement. We also plan to extend the method to distributed memory [74], since the method is cell-wise parallel, allowing us to solve larger problems. We can optimize the method by parametrizing only the polytopal edges and using moment-fitting integration on the surfaces [34]. Further extension of the method involves solving boundary layer problems with a separate discretization, see [30]. Finally, we plan to extend the method to more complex scenarios and practical applications, such as fluid-structure interaction (FSI) and transient problems.

ACKNOWLEDGMENTS

This research was partially funded by the Australian Government through the Australian Research Council (project numbers DP210103092 and DP220103160). We acknowledge Grant PID2021-123611OB-I00 funded by MCIN/AEI/10.13039/501100011033 and by ERDF “A way of making Europe”. P.A. Martorell acknowledges the support received from Universitat Politècnica de Catalunya and Santander Bank through an FPI fellowship (FPI-UPC 2019). This work was also supported by computational resources provided by the Australian Government through NCI under the National Computational Merit Allocation Scheme.

REFERENCES

- [1] T. Hughes, J. Cottrell, and Y. Bazilevs. Isogeometric analysis: CAD, finite elements, NURBS, exact geometry and mesh refinement. *Computer Methods in Applied Mechanics and Engineering*, 194(39-41):4135–4195, oct 2005. doi:[10.1016/j.cma.2004.10.008](https://doi.org/10.1016/j.cma.2004.10.008).
- [2] V. Karypis, George; Kumar. Metis: A software package for partitioning unstructured graphs, partitioning meshes, and computing fill-reducing orderings of sparse matrices. Technical report, University of Minnesota, Department of Computer Science and Engineering, 1997. Available at <https://hdl.handle.net/11299/215346>.
- [3] A. Düster, J. Parvitzian, Z. Yang, and E. Rank. The finite cell method for three-dimensional problems of solid mechanics. *Computer Methods in Applied Mechanics and Engineering*, 197(45-48):3768–3782, Aug. 2008. doi:[10.1016/j.cma.2008.02.036](https://doi.org/10.1016/j.cma.2008.02.036).

- [4] S. Badia, P. A. Martorell, and F. Verdugo. Geometrical discretisations for unfitted finite elements on explicit boundary representations. *Journal of Computational Physics*, 460:111162, jul 2022. doi:[10.1016/j.jcp.2022.111162](https://doi.org/10.1016/j.jcp.2022.111162).
- [5] T.-P. Fries and S. Omerović. Higher-order accurate integration of implicit geometries. *International Journal for Numerical Methods in Engineering*, 106(5):323–371, oct 2015. doi:[10.1002/nme.5121](https://doi.org/10.1002/nme.5121).
- [6] G. Legrain and N. Moës. Adaptive anisotropic integration scheme for high-order fictitious domain methods: Application to thin structures. *International Journal for Numerical Methods in Engineering*, 114(8):882–904, feb 2018. doi:[10.1002/nme.5769](https://doi.org/10.1002/nme.5769).
- [7] T. Fries and D. Schöllhammer. Higher-order meshing of implicit geometries, part II: Approximations on manifolds. *Computer Methods in Applied Mechanics and Engineering*, 326:270–297, nov 2017. doi:[10.1016/j.cma.2017.07.037](https://doi.org/10.1016/j.cma.2017.07.037).
- [8] T. Fries. Higher-order conformal decomposition FEM (CDFEM). *Computer Methods in Applied Mechanics and Engineering*, 328:75–98, jan 2018. doi:[10.1016/j.cma.2017.08.046](https://doi.org/10.1016/j.cma.2017.08.046).
- [9] J. W. Stanford and T. P. Fries. Higher-order accurate meshing of nonsmooth implicitly defined surfaces and intersection curves. *Computational Mathematics and Mathematical Physics*, 59(12): 2093–2107, dec 2019. doi:[10.1134/s0965542519120169](https://doi.org/10.1134/s0965542519120169).
- [10] J. Stanford and T. Fries. A higher-order conformal decomposition finite element method for plane b-rep geometries. *Computers & Structures*, 214:15–27, apr 2019. doi:[10.1016/j.compstruc.2018.12.006](https://doi.org/10.1016/j.compstruc.2018.12.006).
- [11] C. Lehrenfeld. High order unfitted finite element methods on level set domains using isoparametric mappings. *Computer Methods in Applied Mechanics and Engineering*, 300:716–733, Mar. 2016. doi:[10.1016/j.cma.2015.12.005](https://doi.org/10.1016/j.cma.2015.12.005).
- [12] R. I. Saye. High-order quadrature methods for implicitly defined surfaces and volumes in hyperrectangles. *SIAM Journal on Scientific Computing*, 37(2):A993–A1019, Jan. 2015. doi:[10.1137/140966290](https://doi.org/10.1137/140966290).
- [13] F. de Prenter, C. V. Verhoosel, E. H. van Brummelen, M. G. Larson, and S. Badia. Stability and conditioning of immersed finite element methods: Analysis and remedies. *Archives of Computational Methods in Engineering*, 30(6):3617–3656, May 2023. doi:[10.1007/s11831-023-09913-0](https://doi.org/10.1007/s11831-023-09913-0).
- [14] E. Burman. Ghost penalty. *Comptes Rendus Mathématique*, 348(21-22):1217–1220, nov 2010. doi:[10.1016/j.crma.2010.10.006](https://doi.org/10.1016/j.crma.2010.10.006).
- [15] E. Burman, S. Claus, P. Hansbo, M. G. Larson, and A. Massing. CutFEM: Discretizing geometry and partial differential equations. *International Journal for Numerical Methods in Engineering*, 104(7):472–501, dec 2014. doi:[10.1002/nme.4823](https://doi.org/10.1002/nme.4823).
- [16] P. Bastian, C. Engwer, J. Fahlke, and O. Ippisch. An unfitted discontinuous galerkin method for pore-scale simulations of solute transport. *Mathematics and Computers in Simulation*, 81(10): 2051–2061, June 2011. doi:[10.1016/j.matcom.2010.12.024](https://doi.org/10.1016/j.matcom.2010.12.024).
- [17] A. Johansson and M. G. Larson. A high order discontinuous galerkin nitsche method for elliptic problems with fictitious boundary. *Numerische Mathematik*, 123(4):607–628, Sept. 2012. doi:[10.1007/s00211-012-0497-1](https://doi.org/10.1007/s00211-012-0497-1).
- [18] S. Badia, F. Verdugo, and A. F. Martín. The aggregated unfitted finite element method for elliptic problems. *Computer Methods in Applied Mechanics and Engineering*, 336:533–553, jul 2018. doi:[10.1016/j.cma.2018.03.022](https://doi.org/10.1016/j.cma.2018.03.022).
- [19] S. Badia, A. F. Martín, and F. Verdugo. Mixed aggregated finite element methods for the unfitted discretization of the stokes problem. *SIAM Journal on Scientific Computing*, 40(6):B1541–B1576, jan 2018. doi:[10.1137/18m1185624](https://doi.org/10.1137/18m1185624).
- [20] F. Verdugo, A. F. Martín, and S. Badia. Distributed-memory parallelization of the aggregated unfitted finite element method. *Computer Methods in Applied Mechanics and Engineering*, 357:112583, dec 2019. doi:[10.1016/j.cma.2019.112583](https://doi.org/10.1016/j.cma.2019.112583).
- [21] S. Badia, A. F. Martín, E. Neiva, and F. Verdugo. The aggregated unfitted finite element method on parallel tree-based adaptive meshes. *SIAM Journal on Scientific Computing*, 43(3):C203–C234, jan 2021. doi:[10.1137/20m1344512](https://doi.org/10.1137/20m1344512).
- [22] E. Neiva and S. Badia. Robust and scalable h-adaptive aggregated unfitted finite elements for interface elliptic problems. *Computer Methods in Applied Mechanics and Engineering*, 380:113769, jul 2021. doi:[10.1016/j.cma.2021.113769](https://doi.org/10.1016/j.cma.2021.113769).
- [23] S. Badia, E. Neiva, and F. Verdugo. Robust high-order unfitted finite elements by interpolation-based discrete extension. *Computers & Mathematics with Applications*, 127:105–126, dec 2022.

- doi:[10.1016/j.camwa.2022.09.027](https://doi.org/10.1016/j.camwa.2022.09.027).
- [24] S. Badia, E. Neiva, and F. Verdugo. Linking ghost penalty and aggregated unfitted methods. *Computer Methods in Applied Mechanics and Engineering*, 388:114232, jan 2022. doi:[10.1016/j.cma.2021.114232](https://doi.org/10.1016/j.cma.2021.114232).
 - [25] L. Engvall and J. A. Evans. Isogeometric triangular bernstein–bézier discretizations: Automatic mesh generation and geometrically exact finite element analysis. *Computer Methods in Applied Mechanics and Engineering*, 304:378–407, jun 2016. doi:[10.1016/j.cma.2016.02.012](https://doi.org/10.1016/j.cma.2016.02.012).
 - [26] L. Engvall and J. A. Evans. Isogeometric unstructured tetrahedral and mixed-element bernstein–bézier discretizations. *Computer Methods in Applied Mechanics and Engineering*, 319:83–123, jun 2017. doi:[10.1016/j.cma.2017.02.017](https://doi.org/10.1016/j.cma.2017.02.017).
 - [27] S. Xia and X. Qian. Isogeometric analysis with bézier tetrahedra. *Computer Methods in Applied Mechanics and Engineering*, 316:782–816, apr 2017. doi:[10.1016/j.cma.2016.09.045](https://doi.org/10.1016/j.cma.2016.09.045).
 - [28] S. Xia and X. Qian. Generating high-quality high-order parameterization for isogeometric analysis on triangulations. *Computer Methods in Applied Mechanics and Engineering*, 338:1–26, aug 2018. doi:[10.1016/j.cma.2018.04.011](https://doi.org/10.1016/j.cma.2018.04.011).
 - [29] D. Thomas, M. Scott, J. Evans, K. Tew, and E. Evans. Bézier projection: A unified approach for local projection and quadrature-free refinement and coarsening of NURBS and t-splines with particular application to isogeometric design and analysis. *Computer Methods in Applied Mechanics and Engineering*, 284:55–105, feb 2015. doi:[10.1016/j.cma.2014.07.014](https://doi.org/10.1016/j.cma.2014.07.014).
 - [30] X. Wei, B. Marussig, P. Antolin, and A. Buffa. Immersed boundary-conformal isogeometric method for linear elliptic problems. *Computational Mechanics*, 68(6):1385–1405, aug 2021. doi:[10.1007/s00466-021-02074-6](https://doi.org/10.1007/s00466-021-02074-6).
 - [31] P. Antolin, X. Wei, and A. Buffa. Robust numerical integration on curved polyhedra based on folded decompositions. *Computer Methods in Applied Mechanics and Engineering*, 395:114948, may 2022. doi:[10.1016/j.cma.2022.114948](https://doi.org/10.1016/j.cma.2022.114948).
 - [32] P. Antolin and T. Hirschler. Quadrature-free immersed isogeometric analysis. *Engineering with Computers*, 38(5):4475–4499, apr 2022. doi:[10.1007/s00366-022-01644-3](https://doi.org/10.1007/s00366-022-01644-3).
 - [33] E. B. Chin and N. Sukumar. An efficient method to integrate polynomials over polytopes and curved solids. *Computer Aided Geometric Design*, 82:101914, oct 2020. doi:[10.1016/j.cagd.2020.101914](https://doi.org/10.1016/j.cagd.2020.101914).
 - [34] D. Gunderman, K. Weiss, and J. A. Evans. High-accuracy mesh-free quadrature for trimmed parametric surfaces and volumes. *Computer-Aided Design*, 141:103093, dec 2021. doi:[10.1016/j.cad.2021.103093](https://doi.org/10.1016/j.cad.2021.103093).
 - [35] Y. Park, S.-H. Son, M.-S. Kim, and G. Elber. Surface–surface-intersection computation using a bounding volume hierarchy with osculating toroidal patches in the leaf nodes. *Computer-Aided Design*, 127:102866, oct 2020. doi:[10.1016/j.cad.2020.102866](https://doi.org/10.1016/j.cad.2020.102866).
 - [36] N. M. Patrikalakis and T. Maekawa. *Shape interrogation for computer aided design and manufacturing*. Springer Berlin Heidelberg, 2010. doi:[10.1007/978-3-642-04074-0](https://doi.org/10.1007/978-3-642-04074-0).
 - [37] J. Shen, L. Busé, P. Alliez, and N. Dodgson. A line/trimmed NURBS surface intersection algorithm using matrix representations. *Computer Aided Geometric Design*, 48:1–16, nov 2016. doi:[10.1016/j.cagd.2016.07.002](https://doi.org/10.1016/j.cagd.2016.07.002).
 - [38] X. Li and F. Chen. Exact and approximate representations of trimmed surfaces with NURBS and bézier surfaces. In *2009 11th IEEE International Conference on Computer-Aided Design and Computer Graphics*. IEEE, aug 2009. doi:[10.1109/cadcg.2009.5246888](https://doi.org/10.1109/cadcg.2009.5246888).
 - [39] B. Marussig and T. J. R. Hughes. A review of trimming in isogeometric analysis: Challenges, data exchange and simulation aspects. *Archives of Computational Methods in Engineering*, 25(4): 1059–1127, jun 2017. doi:[10.1007/s11831-017-9220-9](https://doi.org/10.1007/s11831-017-9220-9).
 - [40] G. Beer, B. Marussig, and C. Duenser. Simulation with trimmed models. In *The Isogeometric Boundary Element Method*, pages 185–216. Springer International Publishing, sep 2019. doi:[10.1007/978-3-030-23339-6_10](https://doi.org/10.1007/978-3-030-23339-6_10).
 - [41] F. Massarwi, B. van Sossin, and G. Elber. Untrimming: Precise conversion of trimmed-surfaces to tensor-product surfaces. *Computers & Graphics*, 70:80–91, feb 2018. doi:[10.1016/j.cag.2017.08.009](https://doi.org/10.1016/j.cag.2017.08.009).
 - [42] F. Massarwi, P. Antolin, and G. Elber. Volumetric untrimming: Precise decomposition of trimmed trivariates into tensor products. *Computer Aided Geometric Design*, 71:1–15, may 2019. doi:[10.1016/j.cagd.2019.04.005](https://doi.org/10.1016/j.cagd.2019.04.005).

- [43] P. Antolin, A. Buffa, and M. Martinelli. Isogeometric analysis on v-reps: First results. *Computer Methods in Applied Mechanics and Engineering*, 355:976–1002, oct 2019. doi:[10.1016/j.cma.2019.07.015](https://doi.org/10.1016/j.cma.2019.07.015).
- [44] F. Scholz and B. Jüttler. Numerical integration on trimmed three-dimensional domains with implicitly defined trimming surfaces. *Computer Methods in Applied Mechanics and Engineering*, 357:112577, dec 2019. doi:[10.1016/j.cma.2019.112577](https://doi.org/10.1016/j.cma.2019.112577).
- [45] M. J. Borden, M. A. Scott, J. A. Evans, and T. J. R. Hughes. Isogeometric finite element data structures based on bézier extraction of NURBS. *International Journal for Numerical Methods in Engineering*, 87(1-5):15–47, aug 2010. doi:[10.1002/nme.2968](https://doi.org/10.1002/nme.2968).
- [46] B. Mourrain, F. Rouillier, and M.-F. Roy. Bernstein’s basis and real root isolation. Research Report RR-5149, INRIA, 2004.
- [47] M. Reuter, T. S. Mikkelsen, E. C. Sherbrooke, T. Maekawa, and N. M. Patrikalakis. Solving nonlinear polynomial systems in the barycentric bernstein basis. *The Visual Computer*, 24(3):187–200, nov 2007. doi:[10.1007/s00371-007-0184-x](https://doi.org/10.1007/s00371-007-0184-x).
- [48] B. Mourrain and J. Pavone. Subdivision methods for solving polynomial equations. *Journal of Symbolic Computation*, 44(3):292–306, mar 2009. doi:[10.1016/j.jsc.2008.04.016](https://doi.org/10.1016/j.jsc.2008.04.016).
- [49] C. F. Borges and T. Pastva. Total least squares fitting of bézier and b-spline curves to ordered data. *Computer Aided Geometric Design*, 19(4):275–289, apr 2002. doi:[10.1016/s0167-8396\(02\)00088-2](https://doi.org/10.1016/s0167-8396(02)00088-2).
- [50] T. Belytschko, N. Moës, S. Usui, and C. Parimi. Arbitrary discontinuities in finite elements. *International Journal for Numerical Methods in Engineering*, 50(4):993–1013, 2001. doi:[10.1002/1097-0207\(20010210\)50:4<993::aid-nme164>3.0.co;2-m](https://doi.org/10.1002/1097-0207(20010210)50:4<993::aid-nme164>3.0.co;2-m).
- [51] D. Schillinger, P. K. Ruthala, and L. H. Nguyen. Lagrange extraction and projection for NURBS basis functions: A direct link between isogeometric and standard nodal finite element formulations. *International Journal for Numerical Methods in Engineering*, 108(6):515–534, feb 2016. doi:[10.1002/nme.5216](https://doi.org/10.1002/nme.5216).
- [52] B. Müller, S. Krämer-Eis, F. Kummer, and M. Oberlack. A high-order discontinuous galerkin method for compressible flows with immersed boundaries. *International Journal for Numerical Methods in Engineering*, 110(1):3–30, nov 2016. doi:[10.1002/nme.5343](https://doi.org/10.1002/nme.5343).
- [53] C. Geuzaine and J.-F. Remacle. Gmsh: A 3-d finite element mesh generator with built-in pre- and post-processing facilities. *International Journal for Numerical Methods in Engineering*, 79(11):1309–1331, may 2009. doi:[10.1002/nme.2579](https://doi.org/10.1002/nme.2579).
- [54] D. N. Arnold. *Finite Element Exterior Calculus*. Society for Industrial and Applied Mathematics, Dec. 2018. doi:[10.1137/1.9781611975543](https://doi.org/10.1137/1.9781611975543).
- [55] I. Wald and V. Havran. On building fast kd-trees for ray tracing, and on doing that in $O(n \log n)$. In *2006 IEEE Symposium on Interactive Ray Tracing*, pages 61–69. IEEE, 2006.
- [56] C. Ericson. *Real-time collision detection*. Crc Press, 2004.
- [57] G. M. Ziegler. *Lectures on Polytopes*. Springer New York, 1995. doi:[10.1007/978-1-4613-8431-1](https://doi.org/10.1007/978-1-4613-8431-1).
- [58] T. Sorgente, S. Biasotti, and M. Spagnuolo. A geometric approach for computing the kernel of a polyhedron. *Smart Tools and Apps for Graphics - Eurographics Italian Chapter Conference*, 2021. doi:[10.2312/STAG.20211470](https://doi.org/10.2312/STAG.20211470).
- [59] R. Schmidt, R. Wüchner, and K.-U. Bletzinger. Isogeometric analysis of trimmed NURBS geometries. *Computer Methods in Applied Mechanics and Engineering*, 241-244:93–111, oct 2012. doi:[10.1016/j.cma.2012.05.021](https://doi.org/10.1016/j.cma.2012.05.021).
- [60] J. Klosowski, M. Held, J. Mitchell, H. Sowizral, and K. Zikan. Efficient collision detection using bounding volume hierarchies of k-DOPs. *IEEE Transactions on Visualization and Computer Graphics*, 4(1):21–36, 1998. doi:[10.1109/2945.675649](https://doi.org/10.1109/2945.675649).
- [61] X. Xiao, M. Sabin, and F. Cirak. Interrogation of spline surfaces with application to isogeometric design and analysis of lattice-skin structures. *Computer Methods in Applied Mechanics and Engineering*, 351:928–950, jul 2019. doi:[10.1016/j.cma.2019.03.046](https://doi.org/10.1016/j.cma.2019.03.046).
- [62] J. Bezanson, A. Edelman, S. Karpinski, and V. B. Shah. Julia: A fresh approach to numerical computing. *SIAM Review*, 59(1):65–98, jan 2017. doi:[10.1137/141000671](https://doi.org/10.1137/141000671).
- [63] S. Badia and F. Verdugo. Gridap: An extensible finite element toolbox in julia. *Journal of Open Source Software*, 5(52):2520, aug 2020. doi:[10.21105/joss.02520](https://doi.org/10.21105/joss.02520).
- [64] F. Verdugo and S. Badia. The software design of gridap: A finite element package based on the julia JIT compiler. *Computer Physics Communications*, 276:108341, jul 2022. doi:[10.1016/j.cpc.2022.108341](https://doi.org/10.1016/j.cpc.2022.108341).

- [65] F. Verdugo, E. Neiva, and S. Badia. GridapEmbedded. Version 0.8., Jan. 2023. Available at <https://github.com/gridap/GridapEmbedded.jl>.
- [66] P. A. Martorell, S. Badia, and F. Verdugo. STLCutters, Sept. 2021. doi:[10.5281/zenodo.5444427](https://doi.org/10.5281/zenodo.5444427).
- [67] J. Heiskala. DirectQhull. Version 0.2.0., Dec. 2022. Available at <https://github.com/JuhaHeiskala/DirectQhull.jl>.
- [68] C. B. Barber, D. P. Dobkin, and H. Huhdanpaa. The quickhull algorithm for convex hulls. *ACM Transactions on Mathematical Software*, 22(4):469–483, dec 1996. doi:[10.1145/235815.235821](https://doi.org/10.1145/235815.235821).
- [69] F. Verdugo. GridapGmsh. Version 0.6.1., July 2022. Available at <https://github.com/gridap/GridapGmsh.jl>.
- [70] Open cascade technology, 2022. Available at <https://dev.opencascade.org/>, Accessed: Jan, 2023.
- [71] Grabcad, 2023. Available at <https://grabcad.com/library/connecting-rod-416>, Accessed: May, 2023.
- [72] A. Bower. Continuum mechanics, elasticity. *Brown Universit, School of Engineering*, 2012. Available at <https://www.brown.edu/Departments/Engineering/Courses/En221/Notes/Elasticity/Elasticity.htm>, Accessed: May, 2023.
- [73] E. B. Chin, J. B. Lasserre, and N. Sukumar. Numerical integration of homogeneous functions on convex and nonconvex polygons and polyhedra. *Computational Mechanics*, 56(6):967–981, Oct. 2015. doi:[10.1007/s00466-015-1213-7](https://doi.org/10.1007/s00466-015-1213-7).
- [74] S. Badia, A. F. Martín, and F. Verdugo. GridapDistributed: a massively parallel finite element toolbox in julia. *Journal of Open Source Software*, 7(74):4157, jun 2022. doi:[10.21105/joss.04157](https://doi.org/10.21105/joss.04157).